Force variation within arrays of monodisperse spherical particles

G. Akiki, T. L. Jackson, and S. Balachandar
Department of Mechanical and Aerospace Engineering, University of Florida, Gainesville, Florida 32611, USA
(Received 13 February 2016; published 17 August 2016)

This study presents a direct numerical simulation analysis of the force distribution within a cluster of monodisperse spherical particles. A direct forcing immersed boundary method is used to calculate the forces on individual particles for a volume fraction range of $0.11 \leqslant \phi \leqslant 0.44$ and a Reynolds number range of $1.47 \leqslant \mathrm{Re} \leqslant 636$. The hydrodynamic streamwise force is shown to have a normal distribution with a standard deviation ratio to the mean drag that decreases with increasing volume fraction and ranges between 17% and 26%. The lift forces also follow a normal distribution that has a significant standard deviation to mean drag ratio of around 14.5%, which does not vary significantly with the Reynolds number and volume fraction. A model is introduced that adds the identified normal distribution of the forces to the quasisteady force used in point-particle models. A nonisotropic method of defining spatial parameters is presented. It highlights the contribution of each parameter to the variation of the forces on each particle. The results show that the drag is influenced by the closest four to eight neighboring spheres. The drag force is highly dependent on the streamwise distances of the spheres located upstream. For low volume fractions and Reynolds number, the lateral distances of the spheres located downstream also have a significant contribution to those variations. The results also show that the lateral force variation is mostly dictated by the lateral distance of one to two spheres located upstream of each sphere.

DOI: 10.1103/PhysRevFluids.1.044202

I. INTRODUCTION

Porous media have been the subject of much research. Their importance lies in many industrial applications, including soil mechanics, petroleum geology, energy generation, and chemical processes [1]. Numerical investigation of these fluid-solid flows has been on the rise due to the relatively inexpensive studies compared to experimental approaches, the ability to probe inside the pores and gaps, and the ability to cover a wide range of parameters that govern the flow.

Eulerian-Eulerian (EE) or Eulerian-Lagrangian (EL) methods are widely used to simulate particle-laden multiphase flows at the macroscale. The EE method treats the different phases as separate continua. The mass and momentum are conserved for each phase separately. The exchange of momentum between the phases is accounted for through closure models. On the other hand, the EL approach keeps track of the location of point particles by solving the equations of motion. The force on the particles within each cell is calculated using semiempirical point-particle force models, which include the quasisteady standard drag, pressure gradient, added mass, and Basset history forces. Gravitational and lift forces can be added if needed. Unlike the EE approach, the EL one does not have a Stokes number restriction. A more detailed overview of the different methods can be found in Ref. [2].

In a dispersed multiphase flow there are several length scales of importance. The length scales arising from the particles are the particle size (taken to be the diameter d) and the mean interparticle distance l, which goes as $\phi^{-1/3}$, where ϕ is the local particle volume fraction. Note that even at a dilute volume fraction of 1%, the mean nearest-neighbor distance is only 3.7 times the particle diameter. Thus, at moderate volume fractions of interest here, we can take the nearest-neighbor distance to be of the order of the particle diameter. In a turbulent flow the length scale in the continuous phase ranges from the Kolmogorov scale η to the integral scale L.

In the limit $d \ll \eta$, the particles are much smaller than the Kolmogorov length scale. In this limit, the Eulerian-Eulerian and Eulerian-Lagrangian approaches simplify considerably. For particles much smaller than the Kolmogorov scale, the particle Reynolds number, based on the particle diameter and relative velocity, can be estimated to be quite small [3,4]. The advantage is that at such low particle Reynolds numbers we have very reliable point-particle force expressions that fully account for the quasisteady, pressure-gradient, added-mass, and Basset history forces [5]. Furthermore, at low Reynolds numbers the effect of volume fraction on the quasisteady force [6] is well understood and can be incorporated into the point-particle model.

In many dispersed multiphase flow applications of interest the particles are larger and as a result their Reynolds number is often orders of magnitude larger than one. Empirical extensions of the point-particle force model that accurately account for the finite-Reynolds-number effect have been developed and widely used in EE and EL multiphase flow simulations [7]. These finite-Reynolds-number empirical point-particle models are however generally limited to an isolated particle or to a very low volume fraction.

For example, the Reynolds-number dependence of the quasisteady drag of an isolated particle is well established and given by the standard drag relation $C_D = 24/\mathrm{Re}(1 + 0.15\,\mathrm{Re}^{0.687})$. A similar expression for the drag force at finite particle volume fraction is highly desired in a number of environmental and engineering problems and as a result this problem has a long history that can be traced to [8,9]. The classic result of [10] expressed the volume fraction effect as a correction factor to the Stokes drag and validated the corrected drag force against sedimentation experiments of a suspension of spherical particles. In an attempt to extend these drag versus volume fraction correlations to finite Reynolds numbers, there have been many recent direct numerical simulations (DNSs) of fully resolved simulations of finite-Reynolds-number flow over a random array of particles. Of particular relevance to the present work are the DNSs of fully resolved flow around several hundred particles over a Reynolds-number range of 0.01–1000 using the lattice Boltzmann (LB) technique [11,12] and immersed boundary methodology (IBM) [13–15]. The primary focus of these studies has been to obtain a reliable expression for the quasisteady drag force as a function of both Reynolds number and volume fraction. Although there was general agreement, there still remains some difference in the results and the resulting drag force expressions.

The effective drag on a dilute random dispersion of spherical particles in the Stokes limit has been considered in terms of the effective sedimentation velocity of the dispersion in the pioneering work of [16]. Subsequent works by Hill *et al.* [6,17] considered the drag force on an array of spheres as a function of the Reynolds number at solid volume fractions up to the close-packed limits. Using Lattice-Boltzmann simulations, they examined the effects of fluid inertia, at moderate Reynolds numbers, on flows in simple cubic, face-centered-cubic, and random arrays of spheres and compared the effect of particle arrangement for the same effective volume fraction.

Dispersed multiphase flows are inherently stochastic. In the turbulent regime part of the fluctuation has its origin in the carrier phase turbulence. However, even in the absence of ambient flow turbulence, there will be fluctuation (i.e., variation from one realization of the flow to another) arising from the random distribution of particles. This is often called pseudoturbulence. In the Eulerian-Eulerian formulation, the governing equations of both phases are averaged over an ensemble or over a suitably chosen spatial volume [18–20] and only the averaged equations are solved numerically. If the averaging volume is chosen to be larger than d and η but smaller than L, then part of the carrier phase turbulence remains in the macroscale, which must be computed by solving the averaged equations. The averaging, however, eliminates the details of the flow at the microscale, which involves both pseudoturbulence and carrier phase turbulence at subgrid scales that are smaller than the averaging volume.

The effect of these microscale processes that have been averaged out must be properly accounted for in the macroscale governing equations. Unlike in a single-phase flow, since the averaging process involves both phases, we can identify the need for four kinds of closure models:

(i) The effect of the unresolved carrier phase velocity u'_c on the dynamics of the resolved scale carrier phase motion $\bar{u}_c$ must be modeled. This is the same as the subgrid Reynolds stress in the single-phase large-eddy simulation (LES).

(ii) Similarly, the effect of the subgrid particle motion u'_p on the resolved scale particle dynamics $\bar{u}_p$ appears as the subgrid particle Reynolds stress, which must be modeled.

(iii) The phase coupling between the resolved scale carrier flow $\bar{u}_c$ and the resolved scale particle motion $\bar{u}_p$ gives rise to the average force on the particles, which influences the dynamics of the resolved scale particle motion. This force also back couples to the resolved scale carrier phase momentum equation. Although this macroscale phase coupling involves only the resolved scales, it must nevertheless be modeled in the spirit of point-particle models [21–23].

(iv) The unresolved subgrid scale carrier phase motion u'_c and the unresolved subgrid scale particle motion u'_p will contribute to fluctuations in the force coupling between the phases. In other words, the drag force on individual particles can substantially deviate from that predicted by the average drag law. Subgrid scale motion of both the carrier phase and the particles will contribute to force fluctuation. These force fluctuations can in turn both affect the macroscale particle motion and enhance the microscale particle fluctuation. The force fluctuation also back couples to the carrier phase at both the macro- and microscales. All these effects must be appropriately modeled as well.

Our understanding and ability to model these effects are generally limited to the first and third closure problems listed above. Since the first closure is similar to that in single-phase LES, there is a significant body of knowledge to rely upon. Even here it is possible that the presence of the particulate phase can mediate and affect the interaction of the resolved and the unresolved scales of the carrier phase and thus set the carrier phase subgrid closure in a multiphase flow to be different from that in a single-phase flow. Regarding the second closure listed above, in an Eulerian-Eulerian simulation it may be argued that the closure of the particle phase subgrid stress can be similar to that for the continuous phase. The recent results of [11–15] provide a solid foundation for the third closure problem listed above. Recent LES of multiphase flows [24,25] has modeled the effect of unresolved subgrid scale carrier phase motion on particle motion with stochastic forcing, using Langevin-type models. Clearly, further advancement of the above closures requires detailed information on the subgrid scale fluctuations of both the carrier and the particulate phase.

Here we present direct numerical simulations of finite-Reynolds-number flows over a random array of fully resolved monodisperse particles. We vary both the volume fraction of the particles and the average particle Reynolds number. These simulations are similar to those presented in Refs. [11–15]. First we compute the mean drag force on the particle as a function of volume fraction and Reynolds number and obtain good agreement with past results. We build upon this foundation and further investigate the simulation results to address the following additional issues:

(i) The force on the different particles within the random array will deviate from the average value, even in a steady, nominally uniform flow. We will quantify this particle-to-particle force variability and investigate its probability distribution.

(ii) The difference in force experienced by the different particles is due to their random arrangement. The neighborhood of no two particles is the same. Thus the influence of the upstream, downstream, and lateral neighbors is different for every particle. We will correlate the deviation in force from the average value to details of the neighborhood.

(iii) We will investigate if a simple scalar measure, such as local particle volume fraction, around each particle within the random distribution is sufficient to capture the deviation from the average drag.

Even limited answers to the above questions will help us better understand the multiphase closure problem and develop better closure models. The extent of the variation of the quantification and determination of the force variability mentioned in issue (i) is a direct measure of the error introduced by using mean drag models. In this study we quantify the extent of this variation and its probability distribution and suggest a point-particle model that adds a stochastic component to the mean drag model. We further demonstrate the possibility of creating enhanced point-particle models in the future, which can account for the wide variation of the drag and lift forces in a systematic way rather than stochastic forcing. A nonisotropic spatial measure is introduced that can be computed for each sphere based on the relative position of its neighbors. This measure is shown to correlate with the increase or decrease of the hydrodynamic forces on a single particle with respect to the mean.

It must be pointed out that the present simulations are limited to stationary particles. Thus, the effect of subgrid scale fluctuations in particle motion is not included in these simulations. If the particles are allowed to freely move in response to the hydrodynamic force acting on them [26–29], this will result in fluctuating particle velocity, which will couple back to fluctuating forces. In the present simulations the flow over the random array of particles is driven by a uniform streamwise pressure gradient and thus corresponds to a uniform macroscale flow.

The rest of the paper is arranged as follows. In Sec. II the governing equations and the IBM used are presented. The simulation setup and the calculation of the parameters of interest are shown in Sec. III. The numerical convergence and grid independence are presented in Sec. IV. The validation of the current methods is presented in Sec. V. In Sec. VI we present results that show the distribution of the forces within a cluster and the local spatial parameters that best correlate with the force variations. Section VII summarizes the findings and expands to possible future work.

II. GOVERNING EQUATIONS

The Navier-Stokes equations are solved in a channel containing a random distribution of spherical monodisperse particles. A source term is added in the momentum equation to account for the IBM forcing, which imposes the no-slip and no-penetration boundary conditions on the surface of the particles. The modified Navier-Stokes equations are given by

$$\nabla \cdot \boldsymbol{u} = 0, \tag{2.1}$$

$$\frac{\partial \boldsymbol{u}}{\partial t} + \boldsymbol{u} \cdot \nabla \boldsymbol{u} = \nabla p + \frac{1}{\mathrm{Re}}(\nabla^2 \boldsymbol{u}) + \boldsymbol{f}, \tag{2.2}$$

where $\boldsymbol{u}$ is the nondimensional velocity vector and p is the pressure. The Reynolds number is defined as $\mathrm{Re} = \rho u^* d/\mu$, where u^* is the velocity that renders a pressure gradient in the streamwise direction of unity, d is the diameter of the sphere, and ρ and μ are the density and dynamic viscosity of the fluid, respectively. A schematic of the geometry used is shown in Fig. 1. The particles are generated using a simple random number generator for the low volume fractions of $\phi = 0.1$ and 0.2. As for the dense packs of $\phi = 0.4$, the packing algorithm presented by Matsumura and Jackson [30] is used. In all cases, the spheres are not allowed to touch.

A mixed third-order Runge-Kutta and Crank-Nicolson scheme is used for temporal discretization. An intermediate velocity field is obtained at every time stage by solving the Helmholtz equation. The intermediate velocity field is forced to be divergence free through a pressure correction step.

A uniform mesh with periodic boundary conditions is employed in the streamwise x and spanwise y directions. As for the wall-normal direction z, a nonuniform mesh is defined as

$$z_k = \frac{\arcsin\left[\alpha \cos\left((k-1)\frac{\pi}{N_z - 1}\right)\right]}{\arcsin(\alpha)}, \quad 1 \leqslant k \leqslant N_z, \quad 0 \leqslant \alpha < 1, \tag{2.3}$$

where N_z is the Eulerian grid size in the wall-normal direction and α is a constant that controls the stretching of the grid. For α approaching 1, the mesh approaches a uniform distribution. For $\alpha = 0$, the distribution is known as the Chebyshev-Gauss-Lobatto points. A no-stress boundary condition is enforced at the walls of the channel. A sixth-order compact difference scheme is used in all three directions.

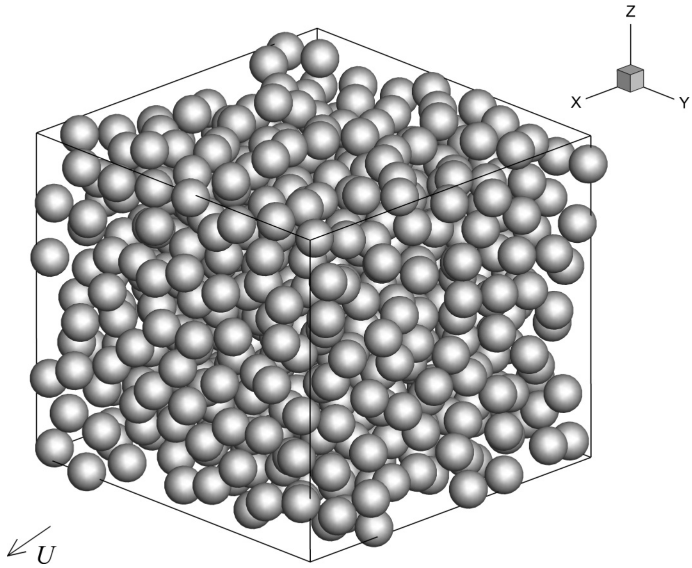

FIG. 1. Schematic of the geometry used.

The immersed boundary (IB) force $\boldsymbol{f}$ is calculated using the method presented in Ref. [26]. The following flow equations are used:

$$\tilde{\boldsymbol{u}} = \boldsymbol{u}^{(m-1)} + c1_m \Delta t[(\boldsymbol{u}\cdot\nabla)\boldsymbol{u}]^{(m-1)} + c1_m c2_m \Delta t[(\boldsymbol{u}\cdot\nabla)\boldsymbol{u}]^{(m-2)} + 2\frac{cd_m}{\mathrm{Re}}\nabla^2\boldsymbol{u}^{(m-1)} - 2cd_m\nabla p^{(m-1)}, \tag{2.4}$$

$$\tilde{\boldsymbol{U}}(\underline{X}_l) = \sum_{\forall \underline{x}} \tilde{\boldsymbol{u}}(\underline{x})\delta(\underline{x} - \underline{X}_l)dv(\underline{x}), \tag{2.5}$$

$$\boldsymbol{F}(\underline{X}_l) = \frac{\boldsymbol{U}(\underline{X}_l)^{(d)} - \tilde{\boldsymbol{U}}(\underline{X}_l)}{\Delta t}, \tag{2.6}$$

$$\boldsymbol{f}(\underline{x}) = \sum_{n=1}^{N_p}\sum_{l=1}^{N_L(n)} \boldsymbol{F}(\underline{X}_l)\delta(\underline{x} - \underline{X}_l)\Delta V_l, \tag{2.7}$$

where cd,$c1$, and $c2$ are the coefficient of diffusion, the coefficient of first nonlinear term, and the coefficient of the second nonlinear term, respectively, and are characteristics of the time advancement scheme used [31,32]. The index m represents the three stages of the temporal scheme. The Eulerian grid nodes and Lagrangian markers are given by $\underline{x}$ and $\underline{X}$, respectively. A preliminary velocity $\tilde{\boldsymbol{u}}$ is calculated in Eq. (2.4). Its Lagrangian counterpart $\tilde{\boldsymbol{U}}$ is obtained through the interpolation step given in Eq. (2.5). Here dv is the volume of the Eulerian grid nodes and δ is the discrete delta function (DDF) [33]. The Lagrangian forcing $\boldsymbol{F}$ needed to enforce the desired velocity $\boldsymbol{U}^{(d)}$ at the immersed interface is calculated on each Lagrangian marker in Eq. (2.6). The Lagrangian forcing is then spread on the Eulerian grid nodes in Eq. (2.7). Here N_p is the number of particles, N_L is the number of Lagrangian markers used for resolving the surface of a sphere [34], and ΔV is the Lagrangian volume assigned to each Lagrangian marker. The markers' distribution and their corresponding volumes are calculated following the methods presented in Ref. [34]. The markers are nonuniformly distributed on the surface of the spheres to match the background Eulerian mesh to keep it optimized. A correction introduced by [35] for the DDF to be used with a nonuniform grid is implemented here. The overall method has been extensively validated for single and multiple spheres, both fixed and moving, and has been shown to recover the hydrodynamic forces accurately (refer to [34]).

III. SIMULATION METHODOLOGY

Flow past a cluster of particles can be accomplished by specifying either a volumetric flow rate or a pressure gradient. In the DNSs of this study, a constant unit pressure gradient is imposed. The volumetric flow rate, and therefore the nondimensional average velocity in the fluid phase u_f, is obtained *a posteriori* as

$$u_f = \frac{1}{(1-\phi)L_x L_y L_z} \int_\Omega I_f(\underline{x})[\boldsymbol{u}(\underline{x}) \cdot \boldsymbol{e}_x] d\underline{x}. \tag{3.1}$$

Here L_i is the dimension of the channel in the ith direction and ϕ is the volume fraction of spheres within

$$I_f(\underline{x}) = \begin{cases} 1 & \text{if } \underline{x} \text{ is the fluid phase} \\ 0 & \text{if } \underline{x} \text{ is the solid phase.} \end{cases} \tag{3.2}$$

The particle Reynolds number is calculated based on the superficial velocity as

$$\mathrm{Re}_p = \frac{\rho(1-\phi)u_f u^* d}{\mu} = (1-\phi)u_f \mathrm{Re}. \tag{3.3}$$

The force on each sphere $\boldsymbol{F}_n$ is then calculated through the integration of the IB forcing obtained from Eq. (2.6),

$$\boldsymbol{F}_n = \sum_{l=1}^{N_L(n)} \boldsymbol{F}(\underline{X}_l)\Delta V_l. \tag{3.4}$$

Since a no-stress boundary condition is used at the top and bottom walls, it can be shown that the total drag on the cluster is equal to the specified pressure gradient multiplied by the total volume of the channel:

$$\sum_{n=1}^{N_p} \boldsymbol{F}_n \cdot \boldsymbol{e}_x = \frac{dp}{dx} L_x L_y L_z, \tag{3.5}$$

where $\boldsymbol{e}_x$ is the unit vector in the x direction. The spheres are distributed randomly inside the channel. The only limitation imposed is that a sphere cannot cross the domain boundary in the wall-normal direction and that every new sphere must be at least a few grid points away from every other sphere. This is only one way to generate a random array of spheres. Another way of generating a random arrangement is through thermal equilibration of a collisional process [13]. Although these different approaches may yield random distribution that agree in the mean volume fraction, they will in general differ in pair and n-particle probability. Figure 2 shows the planar volume fraction variation as a function of z within a channel of height 3π for the cases when the total volume fraction of the whole domain is $\phi = 0.1, 0.2$, and 0.4. The plot is obtained by dividing the domain in the z direction into ten equal subdomains. For each subdomain, we calculate the volume fraction ϕ_z. It can be seen that ϕ_z decreases towards the boundaries of the channel due to the presence of the no-stress walls. This decrease becomes more severe as the volume fraction increases. For all the cases tested, the influence of the walls on the volume fraction is negligible past a distance of two diameters. For consistency, all of the analysis performed in this study is limited to the middle 64th percentile of the channel. In this interior region, the effective average volume fractions are 0.11, 0.21, and 0.44, respectively. We also note that the volume fraction ϕ_z varies by about $\pm 14\%$, $\pm 5\%$, and $\pm 1.8\%$ even in the interior volume for the three cases, respectively. This is due to the finite domain of the numerical setup.

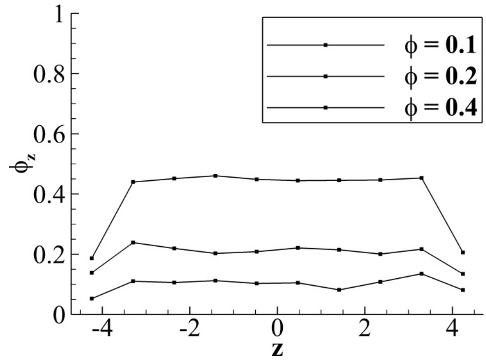

FIG. 2. Planar volume fraction variation with channel height.

IV. GRID INDEPENDENCE AND DOMAIN SIZE

The nonuniform distribution of the Eulerian grid in the wall-normal direction creates a spatially dependent resolution around each sphere. The aim of this study is to investigate the distribution of the hydrodynamic forces within the array of particles. It is crucial therefore to ensure that the variation in the spatial grid along the z direction does not affect the force calculation. A set of particles is placed at the same x and y locations with varying z locations such that the particles are tangent to each other. The limiting case of $\alpha = 0$ is set in Eq. (2.3) to get the maximum difference in particle resolution. Figure 3 shows a schematic of the geometry used. The nonuniform resolution can be clearly identified through the uneven distribution of the Lagrangian markers of each sphere. All the spheres are resolved by 20 grid points along the x and y directions. In the z direction the

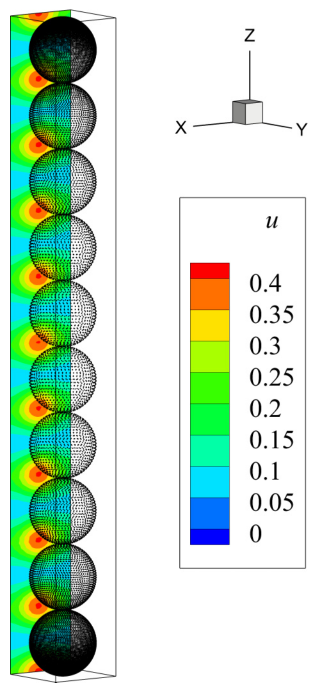

FIG. 3. Schematic of the spatial grid dependence test and the contour plots of the streamwise velocity.

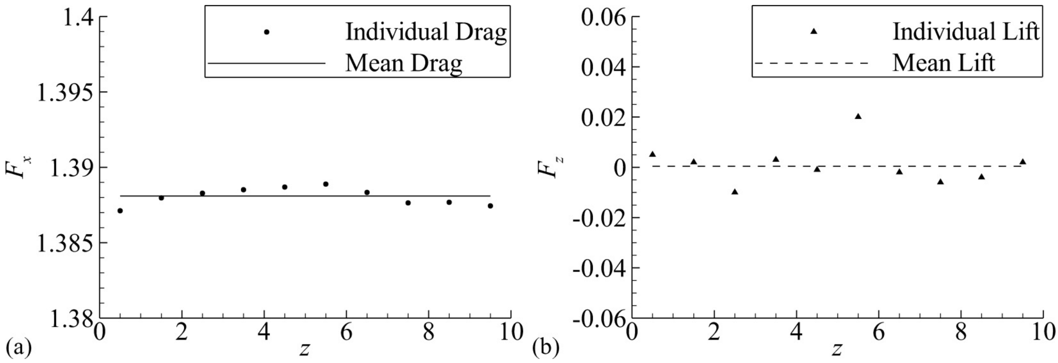

FIG. 4. Individual (a) drag and (b) lift in the z direction on the particles located at different heights in the channel. The maximum deviation of the drag force from the mean drag is 0.067% and the maximum deviation of the lift force from the mean lift is 1.4% with respect to the mean drag.

spheres close to the top and bottom boundaries are resolved by 62 points, while the spheres close to the center plane are resolved by 20 points. The no-stress boundary condition that is applied at the channel walls ensures that all spheres are subject to the same physical condition. Figure 4 shows the values of the hydrodynamic drag and lift in the wall-normal direction on each of the ten particles. The horizontal lines correspond to the mean drag and lift force and are added for reference. For the drag and lift, the maximum deviations from the mean are 0.0674% and 1.4% with respect to the mean drag, respectively. These numbers are small compared to the actual variation of the individual drag and lift on a particle within a random cluster, as shown later.

A set of simulations with varying grid resolution is conducted to investigate the convergence of the overall numerical scheme. The tests are performed for volume fractions of $\phi = 0.2$ and 0.4 at Re $= 10$. A higher Reynolds number of 100 is also tested for a volume fraction of 0.2. The convergence of u_f with an increasing number of grid points per sphere diameter $d/\Delta x$ is shown in Fig. 5. A slower convergence is observed for the higher volume fraction and Reynolds number. A monotonic convergence is observed and for all cases a resolution of $d/\Delta x \geqslant 40$ appears to be adequate.

The size of the computational domain is chosen to be large enough to eliminate any spurious correlation due to the periodic boundary conditions. The minimum length to avoid such autocorrelation can be estimated using the Brinkman screening length [6,36]. This length is typically

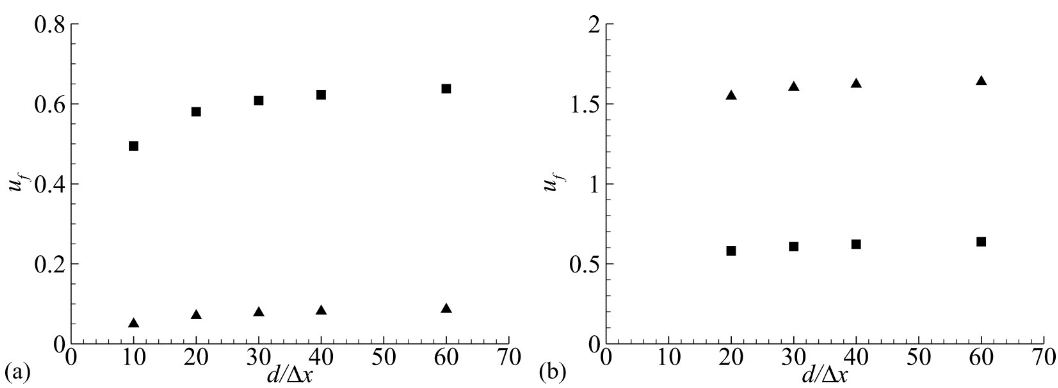

FIG. 5. Grid dependence for (a) $\phi = 0.2(\blacksquare)$ and $\phi = 0.4(\blacktriangle)$ with Re $= 10$ and (b) Re $= 10(\blacksquare)$ and Re $= 100(\blacktriangle)$ with $\phi = 0.2$.

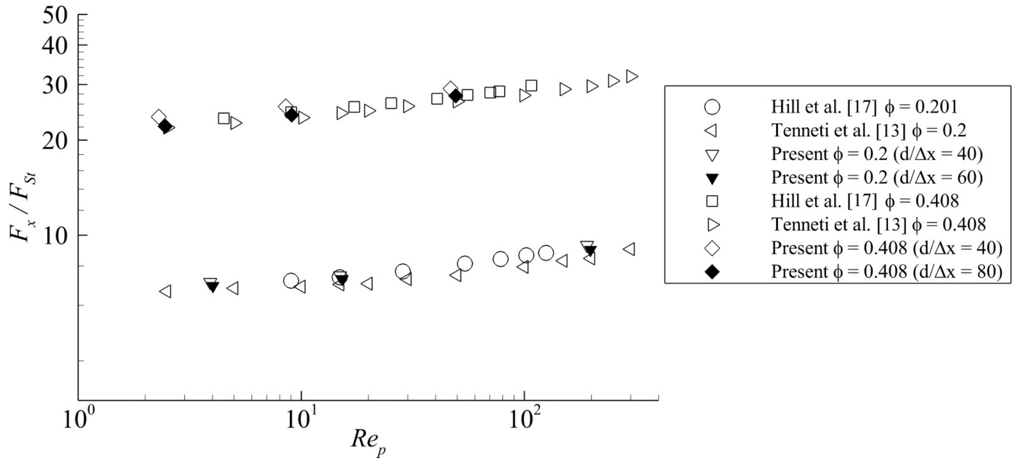

FIG. 6. Normalized drag force versus particle Reynolds number for a sc arrangement of spheres.

much smaller than the extent of fluid disturbance around a single sphere due to the decay caused by the force exerted on the surrounding spheres by the fluid. The higher the volume fraction is, the faster the decay is. Tenneti *et al.* [13] established the decay of the fluid velocity autocorrelation for a volume fraction of 0.2 and Reynolds number of 20 and 300. Their results show that a maximum cubic box of length $2.4d$ is sufficient to avoid autocorrelation. A computational domain of such small size would contain very few spheres. In this study we are interested in obtaining a statistical distribution of the drag and lateral forces on each individual sphere. The statistical variability of the mean and standard deviation of the force distribution would decrease from one realization to another, as more spheres are included in each realization. Here we use a nondimensional domain size of $3\pi \times 3\pi \times 3\pi$.

V. VALIDATION

The IBM and LB techniques have been previously used to simulate the flow over a fixed ordered and random distribution of particles. The fixed particles provide a good approximation for a high-Stokes-number condition for the particles. In this section the current numerical method is validated by comparing the mean drag force on a particle in ordered and random arrays with data from several other studies.

A. Ordered arrays

The flow over a simple cubic (sc) arrangement of spheres at moderate Reynolds number is performed using the present numerical method. The periodic boundary conditions in the x and y directions, along with a symmetry condition in the z direction, simulate a cubic domain of size $L_x = L_y = L_z = d(\pi/6\phi)^{1/3}$, with the particle at its center. Two volume fractions of $\phi = 0.2$ and 0.408 are used. The results are compared in Fig. 6 to data reported by Hill *et al.* [17] using the LB technique and Tenneti *et al.* [13], who employed a variant of the IBM known as the particle-resolved uncontaminated-fluid reconcilable immersed boundary method (PUReIBM). The drag force on the sphere is calculated using Eq. (3.4) as $F_x = \mathbf{F}_n \cdot \mathbf{e}_x$. The forces shown in Fig. 6 are normalized by the Stokes drag F_{St} given by

$$F_{St} = 3\pi\mu d(1-\phi)u_f u^*. \tag{5.1}$$

In the above u_f is the nondimensional velocity, u^* is the velocity scale, and the factor $1-\phi$ is used to obtain the corresponding superficial velocity. For each case, two different resolutions are

TABLE I. Summary of studies on drag correlation for monodisperse static particles.

Study	Re	ϕ	$d/\Delta x$	N_p	NOR
Beetstra *et al.* [11]	20–1000	0.1–0.6	17–26 (LB)	54	1–30
Tenneti *et al.* [13]	0.01–300	0.1–0.5	20–60 (IBM)	20–161	5
Zaidi *et al.* [14]	0.01–1000	0.05–0.5	24–64 (IBM)	95–120	
Bogner *et al.* [12]	0.05–300	0.01–0.35	17–47 (LB)	27,54	5
Tang *et al.* [15]	50–1000	0.1–0.6	12–16 (IBM)	108	10–20
present	1.47–636	0.11–0.44	40–60 (IBM)	108–459	2–5

used: a resolution of $d/\Delta x = 40$ for all cases and higher resolutions of $d/\Delta x = 60$ for $\phi = 0.2$ and $d/\Delta x = 80$ for $\phi = 0.408$. The higher resolution for each case is chosen to match the resolution used by Tenneti *et al.* [13] in their PUReIBM simulations for ordered arrays.

The present results show good agreement with the previous studies. For $\phi = 0.2$, the present results are somewhat between those of [13] and [17]. With higher resolution the ratio slightly decreases by about 2.9%. A similar trend is observed for the larger volume fraction.

B. Random arrays

Many recent studies have investigated the correlation of the mean drag on a sphere as a function of the Reynolds number and volume fraction in a random array of spheres. The most relevant studies are listed in Table I with the ranges of Reynolds number and volume fraction for which the corresponding drag correlation is obtained. Also, the resolution, number of particles per realization N_p and number of realizations (NOR) $\mathcal{N}$ used by each study are included.

1. Comparison of resolution and number of particles

The resolution that is implemented in this study is compared to the other three methods that use IBM. It should be noted that the study by Tang *et al.* [15] employ second-order spatial resolution, but apply an interesting method to correct for the grid size effect [37]. Simulations on ordered face-centered-cubic (fcc) arrays of a low number of particles are performed at very high resolutions for different ϕ for a certain Re_p. The data are extrapolated to obtain an infinite resolution F_d^{fcc}. This result is used to calibrate ϕ at a finite resolution to obtain the resolution free F_d^{fcc}. The volume fraction is then altered by changing the effective diameter in the random array simulations that can now be performed at a lower, more cost effective, resolution. The correction for the finite resolution makes it difficult to quantify the effective order of accuracy. Reference [14] uses a fourth-order central difference scheme with a resolution range that extends to $d/\Delta x = 64$, which is used for the highest Re_p of 1000. For the range of ϕ and Re_p of the present study, the resolution used in Ref. [14] is 40 points per diameter. Similar to [14], the resolution reported in Ref. [13] goes up to $d/\Delta x = 60$. This high resolution is used for the high volume fraction and high-Reynolds-number cases. For the parameters that compare to the ones used in the present study, Ref. [13] uses a grid resolution of $d/\Delta x = 20$, 30, and 40 with a spectrally accurate spatial scheme. Based on these observations, the results to be presented here use $d/\Delta x = 40$ with the sixth-order compact difference scheme. For the highest volume fraction attempted of $\phi = 0.44$, the resolution is increased to $d/\Delta x = 60$. Most importantly, this resolution is more than adequate to reliably obtain the statistics of force variations to be explored here.

Statistical convergence of the mean drag and other parameters of interest also depend on the number of spheres used. Most of the studies in Table I conducted more than one realization to reduce any possible dependence of the mean drag on a specific particle formation. In the present case, two to five realizations are used depending on the volume fraction. We are interested in the hydrodynamic forces on an individual sphere and its variation throughout the cluster. In this context, from a

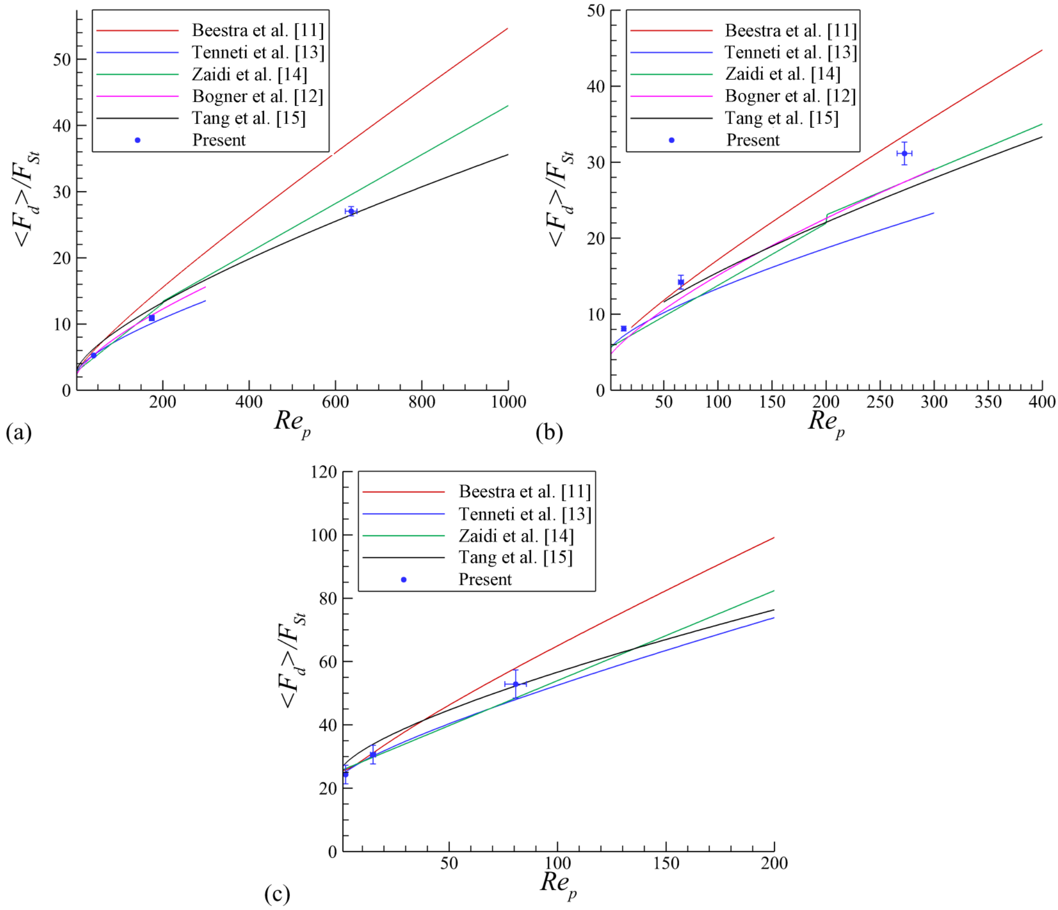

FIG. 7. Drag correlation comparison with present results for (a) $\phi = 0.11$, (b) $\phi = 0.21$, and (c) $\phi = 0.44$ for a random arrangement of spheres.

statistical perspective, each particle is a separate realization since each has a unique neighborhood of surrounding particles. Nonetheless, the total number of spheres used in this study is comparable to the total number of spheres ($N_p \times \mathcal{N}$) used in Refs. [12–14]. It is also large enough to give reliable statistical data with small errors, as will be demonstrated later.

2. Mean drag comparison

Figure 7 shows a comparison of the different drag correlations as a function of the particle Reynolds number for three different volume fractions. Here $\langle F_d \rangle$ is the mean drag calculated from

$$\langle F_d \rangle = \frac{1}{N_p} \sum_{n=1}^{N_p} \boldsymbol{F}_n \cdot \boldsymbol{e}_x. \tag{5.2}$$

Here N_p is the number of particles located in the middle 64% of the channel as explained in Sec. III. The values shown in Fig. 7 are normalized by the Stokes drag given in Eq. (5.1).

The cumulative result of all the prior correlations forms a cone-shaped graph in which the values converge for low Re_p, but the discrepancy increases with increasing Re_p. The lower part of the range of force is bounded by the correlation of [13] for values up to $\mathrm{Re}_p = 300$ and of [15] for $\mathrm{Re}_p > 300$. The upper limit of the force range is the correlation of [11] for all Re_p and ϕ. For the three volume

TABLE II. Summary of cases explored.

Case label	ϕ	Re	Re_p	No. of spheres	NOR
vf1re20	0.11	20	40.10	108	4
vf1re60	0.11	60	174.9	108	4
vf1re180	0.11	180	636.3	108	4
vf2re20	0.21	20	12.98	215	5
vf2re60	0.21	60	68.66	215	2
vf2re180	0.21	180	281.8	215	2
vf3re20	0.44	20	2.28	459	2
vf3re60	0.44	60	14.93	459	2
vf3re180	0.44	180	80.67	459	2

fractions, at $\mathrm{Re}_p = 300$, which is the upper Reynolds-number range of some of the correlations, the drag force varies by 44.35%, 43.51%, and 36.10% with respect to the mean value, respectively. The difference at $\mathrm{Re}_p = 1000$ is 42.69%, 42.97%, and 59.50%, respectively. The source of this wide gap has not been identified and still needs further investigation.

In the present simulations, the flow is pressure driven, therefore the mean velocity u_f is the obtained output. The particle Reynolds number and the normalized force are functions of the mean velocity as shown in Eqs. (3.3) and (5.1). Each realization will give slightly different values of u_f depending on the distribution. The vertical and horizontal error bars shown represent one standard deviation from the mean. The present values of the drag for $\phi = 0.11$ are in good agreement with the correlations given in Refs. [12,13,15]. As for $\phi = 0.21$, the present results fall closer to the correlation reported in Ref. [11]. The Reynolds numbers used at $\phi = 0.44$ are lower than the other two cases. Given the large variation in the mean drag predicted by the different correlation, all we can say is that the current results are consistent with the past investigations, that the present drag results fall within the range of previous data. The wide variation between the different correlations remains an open question. We conjecture that this difference is due to the precise nature of how the spheres are distributed within the computation box. For finite-sized particles, the mean particle volume fraction is not sufficient to describe a uniform distribution of particles. A radial distribution or pair correlation function is also needed to describe the microstructure of the random distribution. For example, for the same mean volume fraction, body centered, face centered, and random arrangements are known to yield substantially different mean drag forces [6,16,17].

VI. RESULTS

In order to study the distribution of the hydrodynamic forces within a cluster of monodisperse spheres, a channel of dimensions $3\pi \times 3\pi \times 3\pi$ is used. Three different volume fractions and Re are considered. The cases and their respective parameters are listed in Table II. The particle Reynolds number Re_p is calculated *a posteriori* using Eq. (3.3). The NOR is determined such that we obtain a sample size of more than 400 particles for each case. For one particular case, vf2re20, more realizations have been performed in order to demonstrate that the results obtained are insensitive to the actual distribution of particles. A resolution of $d/\Delta x = 40$ is employed for the cases of $\phi = 0.1$ and 0.21 and $d/\Delta x$ is set to 60 for the cases with volume fraction equal to 0.44. The coefficient α is set to 0.99 in Eq. (2.3).

The simulations start either from zero initial velocity or with flow field from a different Reynolds number. As a result, the simulations reach a steady or statistically stationary state after an initial transient. Starting at $t = 10$, a cumulative moving average of the difference in the mean velocity u_f inside the channel for consecutive time steps is calculated. At the ith iteration, the mean velocity difference between iterations i and $i - 1$ is added to the moving average, which at that time would represent the average Δu_f for $10 \leqslant t \leqslant t_i$. The data are considered to have reached steady state when the moving average is less than 1×10^{-4}%.

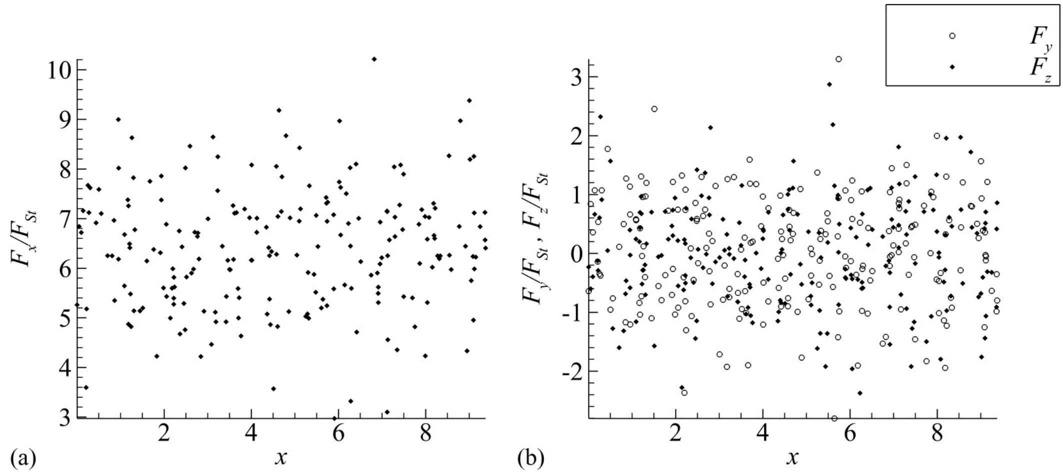

FIG. 8. Scatter plot of the (a) drag and (b) lateral forces versus the streamwise position for case vf2re20.

A. Force distribution

In this section the statistical characteristics of the distribution of the hydrodynamic force on the individual spheres are presented. Figure 8 shows a scatter plot of the drag F_x and lateral forces $F_y = \boldsymbol{F}_n \cdot \boldsymbol{e}_y$ and $F_z = \boldsymbol{F}_n \cdot \boldsymbol{e}_z$ on a single sphere as a function of the streamwise location of the sphere for the case of vf2re20. Both plots show a very significant range of the force scatter. For the case shown, some spheres experience a drag twice as large as some other particles. As for the lateral forces, the range of the scatter is of the same order as the mean drag of the array and therefore cannot be neglected.

The mean and standard deviation for each case is calculated. Table III contains the mean, standard deviation, skewness, and kurtosis of the drag force of the data. The skewness $\mathcal{S}$ and kurtosis $\mathcal{K}$ are calculated as

$$\mathcal{S} = \frac{\frac{1}{N_p}\sum_{i=1}^{N_p}[F(i) - \langle F\rangle]^3}{\sigma^3}, \tag{6.1}$$

$$\mathcal{K} = \frac{\frac{1}{N_p}\sum_{i=1}^{N_p}[F(i) - \langle F\rangle]^4}{\sigma^4}. \tag{6.2}$$

The skewness and kurtosis being close to zero and three, respectively, suggests that the scatter of the drag force follows a normal distribution. The small deviation from zero and three, respectively, is attributed to the finite number of spheres from which the statistics was obtained. The ratio of

TABLE III. Statistical parameter of the drag distribution within the cluster of spheres.

Label	$\langle F_d\rangle/F_{\text{St}}$	$\sigma_{F_d}/F_{\text{St}}$	$\sigma_{F_d}/\langle F_d\rangle$	Skewness	Kurtosis
vf1re20	5.24	1.55	25.64%	0.2	3.43
vf1re60	10.89	2.94	23.62%	0.15	3.17
vf1re180	27.03	6.43	20.78%	0.04	3.09
vf2re20	10.18	2.01	19.87%	0.16	3.12
vf2re60	14.21	4.01	23.08%	–0.03	3.07
vf2re180	31.14	9.11	23.79%	–0.01	2.95
vf3re20	24.31	4.15	17.09%	0.23	3.15
vf3re60	30.60	5.49	17.95%	0.20	3.15
vf3re180	52.86	10.75	20.34%	0.19	3.01

TABLE IV. Statistical parameter of the lift distribution within the cluster of spheres.

Label	$\langle F_L \rangle / F_{St}$	σ_{F_L} / F_{St}	$\sigma_{F_L} / \langle F_d \rangle$	Skewness	Kurtosis
vf1re20	0.02	0.67	12.81%	–0.07	3.82
vf1re60	–0.02	1.44	13.19%	0.11	3.79
vf1re180	–0.05	3.50	12.94%	–0.05	3.50
vf2re20	–0.01	1.44	14.14%	0.19	3.30
vf2re60	0.04	2.01	14.17%	–0.08	3.93
vf2re180	0.04	4.39	14.11%	–0.03	3.78
vf3re20	–0.05	3.95	16.24%	0.41	4.97
vf3re60	–0.11	4.97	16.24%	0.15	4.00
vf3re180	–0.12	8.51	16.10%	0.15	3.96

the standard deviation to the mean drag ranges between 17% and 26%. The ratio shows an inverse relation with the volume fraction as the average ratio for each volume fraction is observed to decrease as the volume fraction increases. This observation can be shown to satisfy the limiting case of very high volume fraction. In the limit of close packing, every particle will have equal probability of finding upstream, downstream, and lateral neighbors. In a random array, the precise arrangement of neighboring particles does vary from particle to particle. However, the level of difference in their relative arrangement decreases, thus significantly decreasing the drag variation from one particle to another. The standard deviation to drag ratio does not follow a definite pattern with varying Re. For the lowest ϕ, the ratio is decreasing with Re and the opposite trend is seen for the other two values of ϕ.

Table IV presents the mean, standard deviation, skewness, and kurtosis of the lateral force distribution. Here drag is defined as hydrodynamic force in the direction of the mean velocity and lift, or lateral force, is defined as perpendicular to the mean velocity. It must be emphasized that the local velocity around an individual particle may deviate from the mean velocity and thus the definitions of drag and lift are only in the sense of mean velocity. The ratio of the standard deviation to the mean drag seems to vary slightly for all cases. This ratio has a mean of 14.42%. The skewness is close to zero for all the cases. The kurtosis is observed to be higher than 3 ($\sim$3.9). Though the difference is not large enough to suggest a strong deviation from a Gaussian distribution, the larger value may be the result of intermittency. The angle θ of the total lift force orientation on the $y - z$ plane, with respect to the positive y axis, is spread unbiasedly in all directions, as can be seen in the two histograms of Fig. 9. Even though the distribution is not perfectly uniform, the two cases shown reveal a nonsystematic pattern, which can be interpreted as the result of a finite random selection from a uniform distribution.

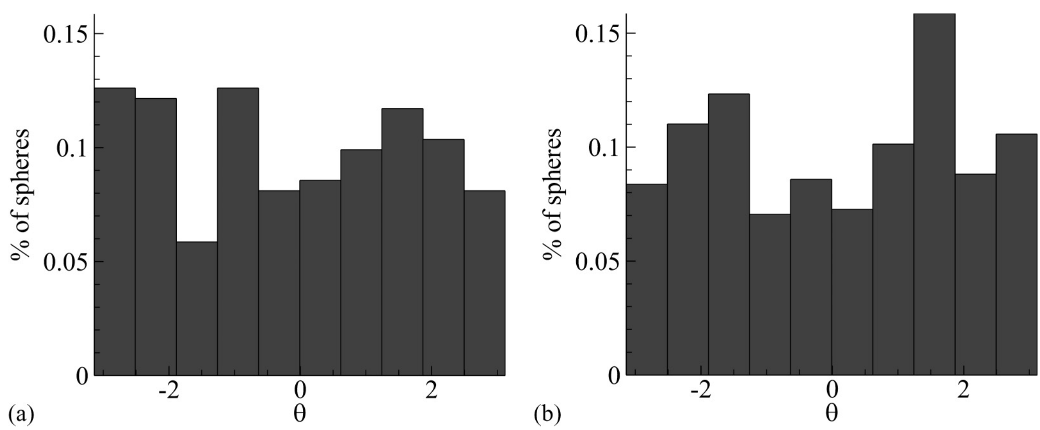

FIG. 9. Histograms of the angle of the lift force distribution for (a) vf2re20 and (b) vf3re60.

TABLE V. Statistical parameter of the drag distribution for different distributions of spheres for vf2re20.

vf2re20	$\langle F_d \rangle / F_{\mathrm{St}}$	$\sigma_{F_d} / F_{\mathrm{St}}$	$\sigma_{F_d} / \langle F_d \rangle$	Skewness	Kurtosis
seed 1	10.26	1.95	19.15%	0.02	3.17
seed 2	10.26	2.15	20.83%	0.24	3.33
seed 3	10.14	2.15	20.93%	0.37	2.84
seed 4	10.18	1.99	19.40%	0.14	3.41
seed 5	10.06	1.82	18.24%	0.03	2.89
mean	10.18 ± 0.08	2.01 ± 0.14		0.16 ± 0.132	3.12 ± 0.229

B. Realization dependence

The case of vf2re20 is repeated for five different sphere distributions by changing the seed of the random number algorithm used in generating the location of the particles. Tables V and VI contain the mean force, standard deviation, skewness, and kurtosis of the drag and lift forces for each of these realizations. With the five realizations for each statistical quantity χ, an average $\bar{\chi}$ and standard error ε_χ can be estimated using

$$\sigma_\chi = \left(\frac{1}{\mathcal{N} - 1} \sum_{n=1}^{\mathcal{N}} (\chi_n - \bar{\chi})^2 \right)^{1/2}, \tag{6.3}$$

$$\varepsilon_\chi = \frac{\sigma_\chi}{\sqrt{\mathcal{N}}}. \tag{6.4}$$

The mean and uncertainty reported in Tables V and VI are $\bar{\chi} \pm 2\varepsilon_\chi$. It can be seen that the estimated uncertainty is low for all the parameters. This is mainly due to the large number of spheres used within each realization, making the statistics less dependent on the specifics of the distribution.

C. Force correlation with local parameters

At this point one can include the statistical information on the force distribution, presented in Sec. VI A, in the quasisteady point-particle drag model as

$$F_{q,s} = \left\{ \langle F_d \rangle (\mathrm{Re}_p, \phi) + N\left[0, \sigma_{F_d}(\mathrm{Re}_p, \phi)\right] \right\} \boldsymbol{e}_r + N\left[0, \sigma_{F_L}(\mathrm{Re}_p, \phi)\right] \boldsymbol{e}_n, \tag{6.5}$$

where $\boldsymbol{e}_r$ is the unit vector along the direction of relative velocity and $\boldsymbol{e}_n$ is a randomly oriented unit vector perpendicular to $\boldsymbol{e}_r$. The mean drag $\langle F_d \rangle$ can be obtained from one of the correlations listed in Sec. V (refer to the Appendix). A fluctuating force is added to each sphere through a random selection from a normal distribution $N[0, \sigma_{F_d}(\mathrm{Re}_p, \phi)]$, with zero mean and a standard deviation, which is dependent on the Reynolds number and volume fraction. Values of σ_{F_d} can be found in Table III. The last term of Eq. (6.5) introduces a random lateral force that is generally neglected in

TABLE VI. Statistical parameter of the spanwise lift distribution for different distributions of spheres for vf2re20.

vf2re20	$\langle F_L \rangle / F_{\mathrm{St}}$	$\sigma_{F_L} / F_{\mathrm{St}}$	$\sigma_{F_L} / \langle F_d \rangle$	Skewness	Kurtosis
seed 1	–0.02773	1.45	14.11%	0.10	3.16
seed 2	-3.7×10^{-4}	1.49	14.52%	0.28	3.74
seed 3	-5.4×10^{-3}	1.53	15.10%	0.193	3.10
seed 4	9.1×10^{-3}	1.37	13.41%	0.34	3.55
seed 5	–0.02	1.41	13.99%	0.04	2.94
mean	$-8.0 \times 10^{-3} \pm 0.05$	1.44 ± 0.06		0.19 ± 0.11	3.30 ± 0.298

most previous models. The lateral force is introduced in a perpendicular direction $\boldsymbol{e}_n$ with respect to the streamwise direction without any bias. The magnitude of the lift force for each sphere is a random sampling from a normal distribution $N[0,\sigma_{F_L}(\mathrm{Re}_p,\phi)]$ with a mean of zero and a standard deviation σ_{F_L} of 14.5% of the mean drag $\langle F_d \rangle$. The point-particle model presented in Eq. (6.5) introduces variation in the drag and lateral forces as observed in the DNSs.

The force on an individual particle deviates from the mean value due to the presence of all other particles. Thus, in principle, the force on every particle should be modeled accurately in terms of the relative location of all other particles. However, point-particle modeling of such an N-body interaction problem is impractical since it can only be achieved, with the current knowledge, through a fully resolved DNS of the exact random distribution of the N particles. A feasible approach is to identify parameters that characterize the local neighborhood of particle arrangement that best correlates with the actual drag and lift forces. Being able to identify those parameters would pave the way to improved models that can better estimate the hydrodynamic forces on each individual particle based on the unique location of its neighbors, which is information that is readily available in EL methods.

1. Local volume fraction

From Fig. 7 it is clear that the mean drag is dependent on the Reynolds number and the volume fraction of the cluster. On a local level, we define the undisturbed flow witnessed by each sphere to be the flow in its absence, but in the presence of all other spheres. This local undisturbed flow for each sphere will deviate from the mean mesoscale continuous phase velocity and this deviation will impose a different drag and lift force on each particle. As far as mesoscale simulations are concerned, this flow field variation within the cluster is at the microscale and therefore not available in either EE or EL simulations. On the contrary, knowing the exact location of the particles allows us to define a local volume fraction around each particle. One definition of the local volume fraction ϕ_L in a random media is given in Ref. [38] as

$$\phi_L = \frac{1}{V_L}\int [1 - I_f(x)] I_L(x) dx. \tag{6.6}$$

Here V_L is the volume of an observation window W_L defined around the center of an individual sphere and I_L is the indicator function of W_L defined as

$$I_L(x) = \begin{cases} 1 & \text{for } x \in W_L \\ 0 & \text{otherwise.} \end{cases} \tag{6.7}$$

A virtual sphere with radius R_L and concentric with the particle of concern is taken as W_L in this case.

The nth-nearest-neighbor distance [30,39] is another parameter that provides a measure of the local volume fraction. In general, this parameter is used as a mean value for the entire cluster and therefore variations due to particle-particle interactions are not considered. For this application, an individual definition is used and for each particle the nth-neighbor distance is given by

$$\gamma_n = (d_n - d)/d, \tag{6.8}$$

where d_n is the distance between the center of a sphere and its nth nearest neighbor and d is the diameter of the particle.

These definitions of local volume fraction have been applied to all the particles in all the cases listed in Table II. In the case of ϕ_L, the outer radius was varied from $R_L = 1$ to $R_L = 4$ and in the case of nth nearest neighbor, n was varied from 1 to 20. A correlation of these local volume fraction parameters and the drag on each particle is quantified as follows. A scatter plot of the local volume fraction around each sphere as the abscissa and the drag on that sphere as the ordinate is plotted (refer to Fig. 10). It can be seen that even though the mean volume fraction in the interior of the domain (away from the top and bottom boundaries) is 0.44, the local volume fraction measured around

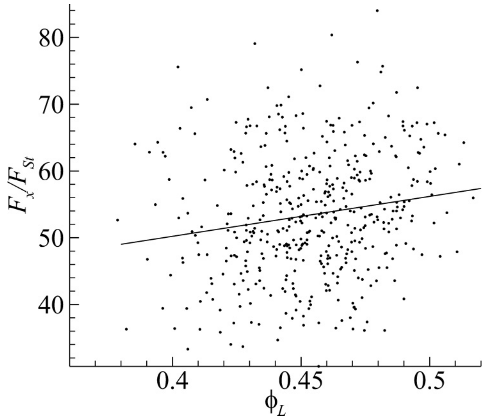

FIG. 10. Scatter plot of drag vs the local volume fraction for case vf3re60 and the linear fit of the data. Here $R^2 = 0.029$ and $R_L = 2$.

the individual spheres ranges from about 0.38 to 0.51, reflecting the random nature of the uniform distribution of spheres. Using linear regression, a line is fitted through the scatter plot. The correlation coefficient R^2 is then computed to serve as an indication of the extent of correlation between the local volume fraction parameter and the actual drag. In all the simulation cases considered, for all the different local volume fraction measures, R^2 reached a maximum of only 0.089, with its value being mostly in the range of 10^{-3}. Figure 10 shows a typical scatter plot of the local volume fraction versus the drag obtained from the DNS of case vf3re60 using $R_L = 2$. It is clear that there is no significant correlation and it is shown here as an example. A scatter plot of the local volume fraction or the nearest-neighbor distance against the lift force on the sphere shows similar results with virtually no correlation between the two quantities.

From the above discussion it is clear that simple measures of local volume fraction and the nearest-neighbor distance are unable to predict the deviation of the actual force on the particle about the mean value. It should be noted that the present simulations, in agreement with past findings, obtain a strong correlation between mean drag and mean volume fraction for the random array as a whole. Based on this, one might expect positive correlation between the local volume fraction and an increase in drag above the mean value. However, such correlation is not observed in any of the cases considered. For the same local volume fraction we observe both an increase and a decrease in drag force, depending on other parameters that go beyond the above simple measures of local volume fraction.

Figure 11 shows two particles (black) with their six closest neighbors. These two particles have exactly the same $\gamma_6 = 0.88$ and their values of ϕ_L are quite close as well at $\phi_L = 0.15$ and 0.12, respectively. The central particle of Fig. 11(a) has a drag force of $F_x = 6.03$, while the one in Fig. 11(b) has a drag $F_x = 1.48$, and the mean drag of the whole cluster is 4.69 (case vf1re60).

(a) 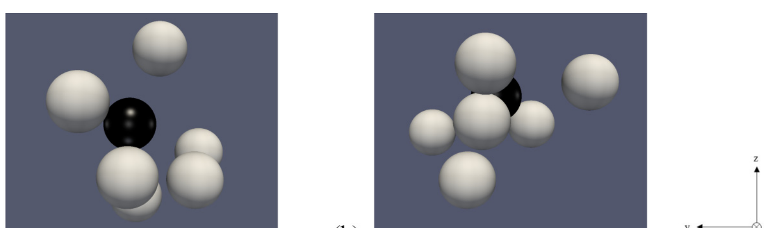 (b)

FIG. 11. Upstream view of the scatter of the six closest neighbors for two different spheres with the same sixth-nearest-neighbor parameter.

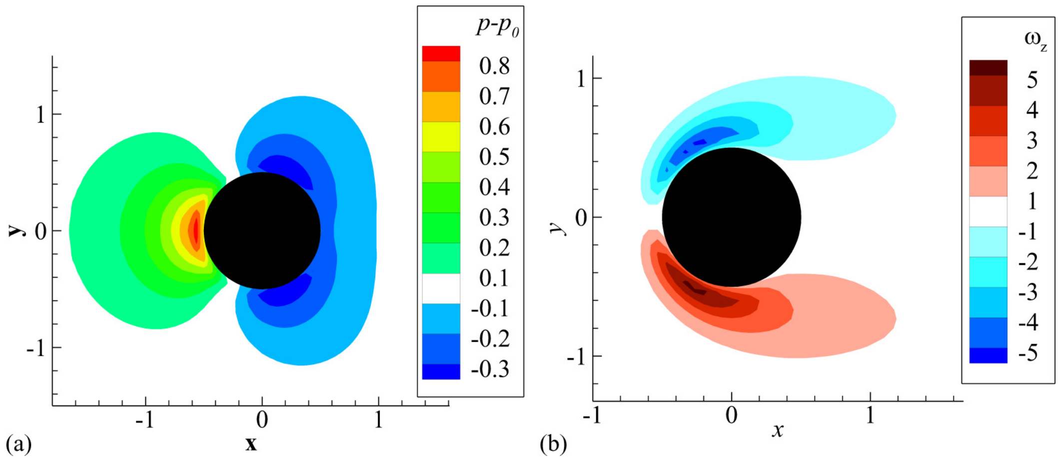

FIG. 12. Instantaneous (a) pressure and (b) vorticity fields over a single sphere in an ambient flow. Here $\mathrm{Re}_p = 16.7$.

The particles are visualized in Fig. 11 from an observer located directly upstream. Even though the distances of the surrounding particles are comparable, the particle in Fig. 11(b) is shadowed from the incoming flow, thus having a drag on the lower end of the drag distribution of the cluster. In contrast, the surrounding particles in Fig. 11(a) seems to funnel the flow towards the central sphere, which results in a higher than average drag.

To better understand the problem, the pressure and vorticity fields are shown in Fig. 12 for a uniform ambient flow over a single spherical particle. In this figure the uniform flow is from left to right. From the figure it can be seen that a particle lying upstream of the one shown will likely witnesses a higher-pressure field in its wake. Similarly, a particle lying downstream of the reference particle shown in Fig. 12(a) will likely experience a lower pressure at the front stagnation point. This suggests that one can expect the role of a neighboring sphere located downstream to be quite different from one located upstream. Also, when it comes to the pressure field, dead spots can be identified at around $\pm 45^\circ$ with the upstream x axis.

The vorticity field, on the other hand, has a smaller radius of influence than the pressure field. Its main effects are concentrated in regions that are different from the pressure field. The highest vorticities are located at an angle upstream where pressure has its mildest influence. A wider influence of the vorticity field can be seen at an angle downstream with little effect on locations directly downstream. When it comes to clusters of particles, the pressure and vorticity effects of all neighboring spheres affect the variation of the drag and lift forces from the mean. This shows the complexity of the problem and that it is nearly impossible to predict the drag on a particle exactly without accounting for the complex effect of all the neighboring particles with a fully resolved DNS.

The above description suggests that this problem should be tackled using a nonisotropic measure of local volume fraction. The presence of particles upstream and downstream must be considered differently and, similarly, the effect of lateral particles must be taken into account appropriately.

2. Nonisotropic measure of neighborhood

The purpose of this subsection is to define an anisotropic measure that quantifies the effective streamwise and transverse distances of neighboring particles in both the upstream and downstream directions. There are different mathematically elegant measures that can be pursued, such as using Minkowski functionals [40]. However, here we use very simple measures that can be readily visualized and understood. Our goal is to show that such anisotropic measures of a local neighborhood have a better correlation with the drag and lift variation than the isotropic measure of a local volume fraction. The simple anisotropic measure to be presented below is sufficient for this demonstration. The cases investigated in this study involve only a monodisperse cluster of particles. Having a fixed diameter for all particles means that the local volume fraction can be interpreted solely in terms of the spacing between the centers of the spheres. We consider m spheres that are closest to the reference sphere i, but located downstream of i, and n spheres that are closest to sphere i, but located upstream of i. Four spatial variables can now be computed as

$$\zeta_{L,d}(i) = \sum_{l=1}^{m} \sqrt{[y(i) - y(l)]^2 + [z(i) - z(l)]^2}, \tag{6.9}$$

$$\zeta_{L,u}(i) = \sum_{l=1}^{n} \sqrt{[y(i) - y(l)]^2 + [z(i) - z(l)]^2}, \tag{6.10}$$

$$\zeta_{S,d}(i) = -\sum_{l=1}^{m} [x(i) - x(l)], \tag{6.11}$$

$$\zeta_{S,u}(i) = \sum_{l=1}^{n} [x(i) - x(l)]. \tag{6.12}$$

The ith sphere has its center located at $[x(i), y(i), z(i)]$. The parameters given in Eqs. (6.9) and (6.10) are measures of the effective lateral displacement of the downstream and upstream neighboring particles, respectively. Similarly, the spatial parameters given by Eqs. (6.11) and (6.12) are measures of the effective streamwise distance separating the center sphere i and the neighboring particles in the downstream and upstream directions, respectively. The negative sign appearing in Eq. (6.11) ensures a positive value of $\zeta_{S,d}$. A sphere l is considered upstream or downstream with respect to sphere i if it satisfies the conditions

$$x(i) - x(l) \geqslant 0, \tag{6.13}$$

$$x(i) - x(l) < 0, \tag{6.14}$$

respectively. A composite parameter X is defined as

$$X(i) = a\zeta_{L,d}(i) + b\zeta_{L,u}(i) + c\zeta_{S,d}(i) + d\zeta_{S,u}(i), \tag{6.15}$$

where a, b, c, and d are weights assigned to each spatial parameter. For simplicity, n is set equal to m for the rest of this study. It should be noted that a radius of influence around each sphere, similar to R_L, which was defined in the previous section, is a more classical way of defining the neighborhood around a particle. In this study, the radius of influence is replaced by a discrete number of neighboring particles. The parameter m allows for the incorporation of the effect of the same number of neighbors (upstream and downstream) irrespective of whether they are close to or away from sphere i, depending on the local volume fraction.

a. Drag correlation. The parameters a, b, c, d, and m are yet to be determined weights in the definition of X given in Eq. (6.15). For each m, through regression we find the best combination of a, b, c, and d that best fits a linear curve onto a scatter plot of X versus the drag ($F_x = \boldsymbol{F}_n \cdot \boldsymbol{e}_x$). The correlation R^2 between the best fit and the scatter plot is calculated. Figure 13 shows the variation of R^2 as a function of m. For $\phi = 0.11$ and 0.21, the highest correlation occurs when $m = 2$. As for $\phi = 0.44$, the value of m that results in the highest correlation seems to decrease with increasing Reynolds number. Table VII summarizes the optimum values of the weights that result in the highest correlation with the actual drag. The values of these weights are a direct indication of the importance of upstream and downstream neighbors in inducing the drag variation. An example of the scatter plot and its corresponding linear fit is shown in Fig. 14 for the case vf2re60. The plot shows that the force tends to increase with increasing X. Together, Table VII and Fig. 14 provide significant insight

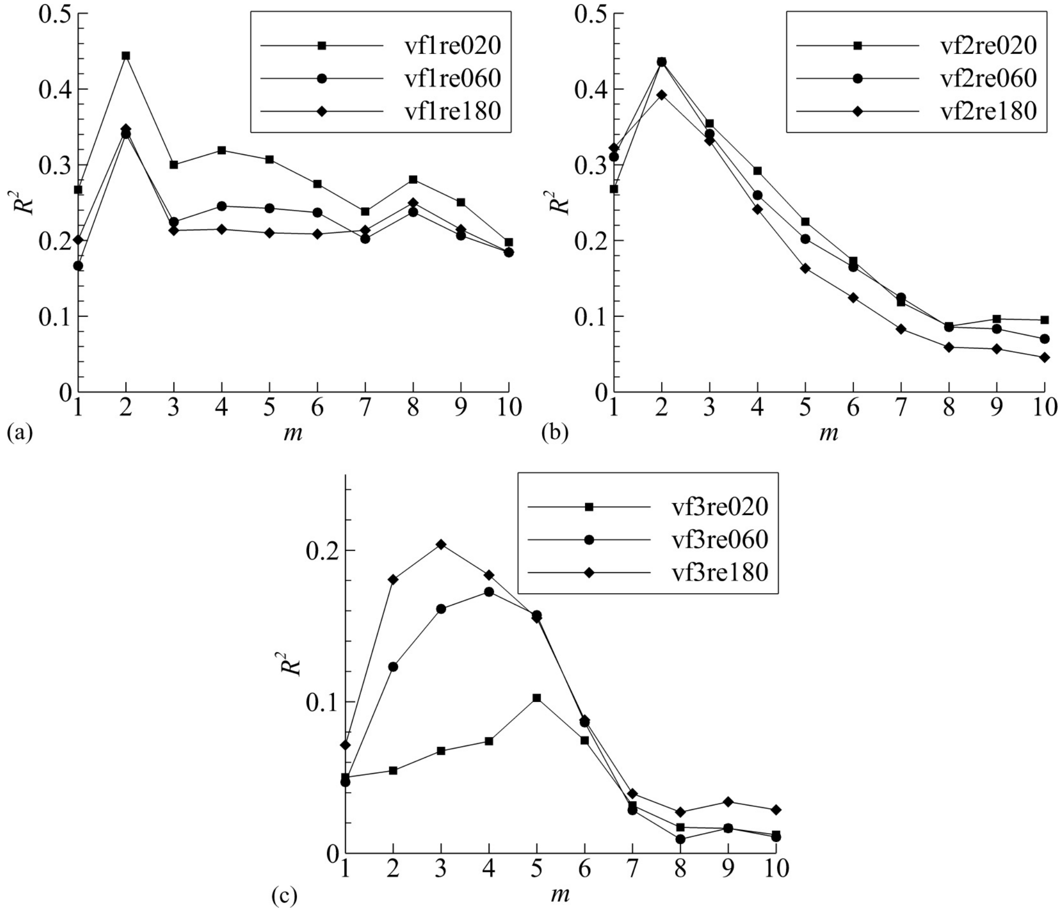

FIG. 13. Maximum coefficient of determination of the drag scatter data as a function of surrounding particles included for (a) $\phi = 0.11$, (b) $\phi = 0.21$, and (c) $\phi = 0.44$.

into the manner each spatial parameter from Eqs. (6.9)–(6.12) contributes to the deviation of the individual drag from the mean drag. Several observations can be extracted from the results shown in Table VII:

TABLE VII. Number of spheres and the weights of the spatial parameters that result in the highest correlation with the drag scatter data.

Case	m	R^2	a	b	c	d
vf1re20	2	0.44	0.75	0	0	−0.25
vf1re60	2	0.22	0.5	−0.1	−0.1	−0.3
vf1re180	2	0.21	0.44	−0.11	−0.11	−0.33
vf2re20	2	0.44	0.42	−0.08	−0.17	−0.33
vf2re60	2	0.44	0.25	−0.17	−0.17	−0.42
vf2re180	2	0.39	0.18	−0.18	−0.18	−0.45
vf3re20	5	0.10	0.09	−0.18	−0.36	−0.36
vf3re60	4	0.17	0.18	0	−0.36	−0.45
vf3re180	3	0.20	0	0.1	−0.4	−0.5

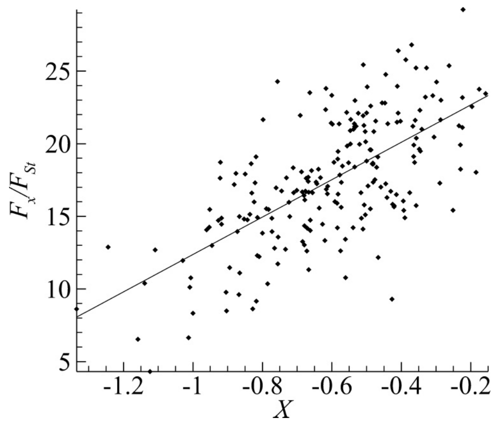

FIG. 14. Scatter plot of the actual drag and X using the parameters listed in Table VII for vf2re60 alongside the linear fit of the data.

(i) Higher correlations are obtained when using nonisotropic measures of local neighborhood than isotropic definitions of volume fraction; recall from Sec. VI C 1 that R^2 is at most 0.089 when using the isotropic definition of volume fraction. However, it must be emphasized that R^2 values are still smaller than 1.0, indicating that the correlation is not perfect. For the highest volume fraction of 40%, the increase in the correlation is not as substantial.

(ii) The weight a is positive for all cases and decreases as the volume fraction and Reynolds number increase. For the cases of low Re and ϕ, the lateral position of the neighboring particles located downstream has the most significant role in determining the variation of the drag on the reference particle. As the lateral gap increases, the drag increases.

(iii) The lateral position of the particles upstream has a marginal role on the drag variation compared to the other spatial parameters since b has a small value in all cases.

(iv) The streamwise gap with the neighboring particles located downstream $\zeta_{S,d}$ has greater influence on the drag variation as the volume fraction increases. The greater the streamwise gap is in the downstream direction, the smaller the drag is.

(v) As can be expected, the upstream separation in the streamwise direction $\zeta_{S,u}$ is the major parameter for all cases. The negative sign of d indicates that as $\zeta_{S,u}$ increases, the drag decreases.

To interpret these observations, we refer to Fig. 12 and compare it to plots of the pressure and vorticity contour obtained from DNS of a uniform ambient flow passing over two spheres shown in Figs. 15 and 16, respectively, where the flow is from left to right. Figures 15(a) and 16(a) have the two particles placed diagonally at a distance of $\{1d, 1d\}$ relative to each other, while Figs. 15(b) and 16(b) have the two particles placed horizontally in the streamwise direction separated by a distance of $1.5d$.

Studies on the interaction between two neighboring spheres goes back to [41,42], which investigated the interaction in the Stokes regime. At low Reynolds numbers the Stokeslet portion of the perturbation decays slowly (as one over the distance) and thus the influence of one sphere on the other extends farther out. At the finite Reynolds numbers considered here the strongest interaction is limited to the immediate neighborhood of each particle. Nevertheless, the qualitative behavior of the interaction is consistent with the classical picture of [41,42].

In Fig. 12 both the pressure and vorticity fields display clear fore-aft asymmetry. This clearly indicates that the effect of the upstream sphere on a downstream sphere will not be same as that of a downstream sphere on an upstream sphere. This asymmetric influence is evident in Figs. 15 and 16. In fact, the drag force on the upstream and downstream spheres in Figs. 15(b) and 16(b) are 1.04 and 0.65, while the drag force on the isolated sphere in Fig. 12 is 1.16. The effect on the particle located downstream is more severe, since the disturbance due to the presence of the front

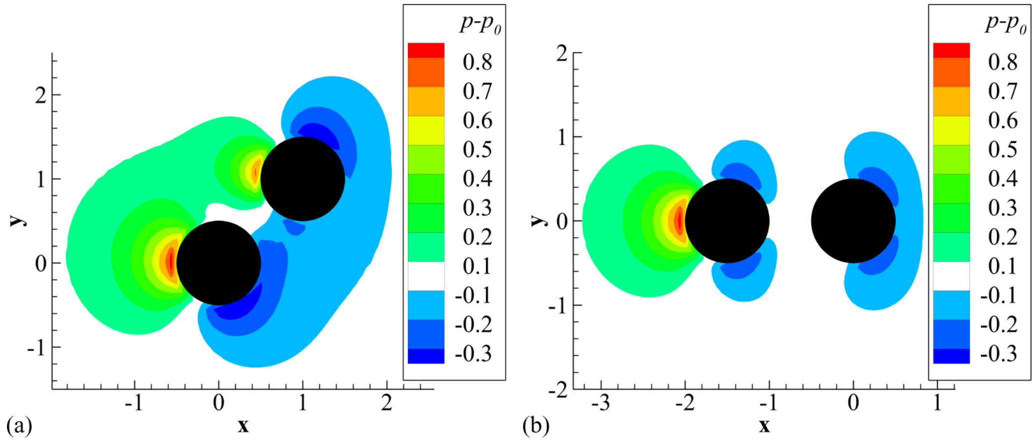

FIG. 15. Instantaneous pressure contour plots around two particles in an ambient flow placed (a) diagonally and (b) horizontally. Here $\mathrm{Re}_p = 16.7$.

particle affects the area of high pressure, which is more significant for a particle. The high-pressure area of the rear particle has been reduced to almost zero. On the other hand, the front sphere has its negative pressure area only partially diminished due to the presence of the rear sphere. In Figs. 15(a) and 16(a), the arrangement of the particles lead to drags of 1.13 and 0.86. The deviation of the drag from the single-particle drag is less severe for this case than the one shown in Figs. 15(b) and 16(b). Nonetheless, the rear particle still witnesses a larger decrease in drag than the front particle due to the effect the presence of the front particle has on the area of high pressure of the rear sphere. Figures 15(a) and 16(a) also show an asymmetry in the lateral direction. Here the front particle has a lateral force of -0.26, while the rear particle has a lateral force of 0.024. The high-pressure area of the rear particle cancels the negative pressure located on the upper side of the front particle, while the presence of the front particle partially disturbs the lower part of the negative pressure area of the rear sphere. While the analysis of the pressure fields can be done for an interaction between a pair of spheres, in a random array of spheres the scenario is far more complicated.

We now refer to the second observation listed above and provide an interpretation. Downstream of the particle, a large value of effective lateral distance indicates that the neighboring particle is not in the direct wake of the reference particle, but located off the streamwise axis. Thus, the larger

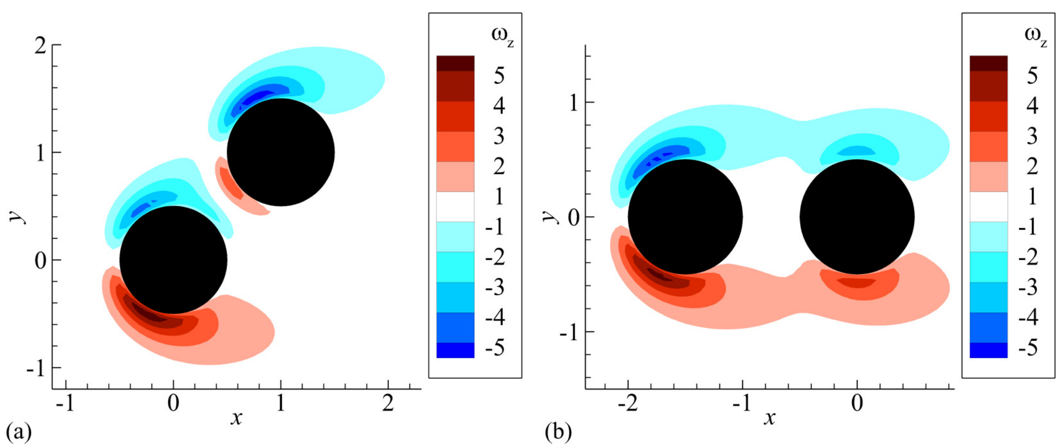

FIG. 16. Instantaneous vorticity contour plots around two particles in an ambient flow placed (a) diagonally and (b) horizontally. Here $\mathrm{Re}_p = 16.7$.

$\zeta_{L,d}$ is, the less the neighboring particles influence the low-pressure wake region of the reference particle, which leads to higher drag. A similar interpretation can be given to the role of the effective lateral distance of the upstream located neighboring spheres. However, the third observation seems to indicate that the role of the lateral location of the upstream spheres is not as significant. As will be shown below, the effect of the upstream located spheres is better reflected in their effective streamwise location.

The negative values of the weights c and d and consequently the fourth and fifth observations listed above may seem somewhat counterintuitive. To properly interpret these observations, the definitions (6.11) and (6.12) along with the definitions of upstream and downstream spheres must be viewed carefully. A small value of $\zeta_{S,d}$ indicates small streamwise separation between the centers of the two spheres. For $\zeta_{S,d} < d/2$, there must be large lateral separation between the two spheres. Thus, if the neighborhood is dominated by spheres in the immediate vicinity (i.e., $\zeta_{S,d} < d/2$) then increasing $\zeta_{S,d}$ corresponds to increasing possibility of smaller lateral separation and contributes to lower drag through the blocking effect. The above argument equally applies to the role of effective streamwise separation of the upstream spheres (i.e., $\zeta_{S,u}$). This explains the negative values of the weights c and d. However, if we limit the upstream and downstream spheres to those that are more than one radius away from the reference sphere, then their lateral positions are not constrained by the volume excluded by the reference sphere. In fact, if we define upstream and downstream spheres as

$$x(i) - x(l) \geqslant d, \tag{6.16}$$

$$x(i) - x(l) < -d \tag{6.17}$$

and recompute the optimal weights (not presented here), we observe all the weights to be positive. In particular, increasing $\zeta_{S,d}$ and $\zeta_{S,u}$ now corresponds to spheres that are farther away from the reference sphere (without any constraint on their lateral position) and thus their influence in reducing the drag on the reference sphere decreases. However, by not including neighbors whose centers are within a radius downstream or upstream of the reference particle, the effect of some of the most influential nearest neighbors is ignored and the corresponding R^2 values are lower.

We stress again the simple nature of the composite parameter X defined in Eq. (6.15). One of the major approximations that X introduces is the linear combination of the spatial measurements. Another approach is to investigate the effects of the streamwise and lateral positions of the neighboring spheres independently. Although this may help us understand the role of neighbors in each direction, the nonlinearity effects and the interaction of the streamwise and lateral positions become more prominent in higher volume fractions.

In an attempt to account for the nonlinear nature of the influence from the surrounding neighbors, higher degree polynomials were tested for the nonisotropic spatial measure rather than the linear combination shown in Eq. (6.15). Also, higher degree polynomials were attempted for the curve fitting instead of the linear fit. No significantly improved correlation was obtained in any of the cases. Therefore, for simplicity, the discussion will be limited to linear models.

b. Lift correlation. The same analysis is applied on the lateral forces and will be discussed below. The definitions given in Eqs. (6.9) and (6.10) are now changed to

$$\zeta_{L,d}(i) = \sum_{l=1}^{m} [y_d(l) - y(i)], \tag{6.18}$$

$$\zeta_{L,u}(i) = \sum_{l=1}^{m} [y_u(l) - y(i)], \tag{6.19}$$

where y_d and y_u are the lateral coordinates of the m closest spheres located downstream and upstream of sphere i, respectively. In the above revised definition of effective lateral separation along the y direction, the contribution from each neighboring particle can be either positive or negative, unlike

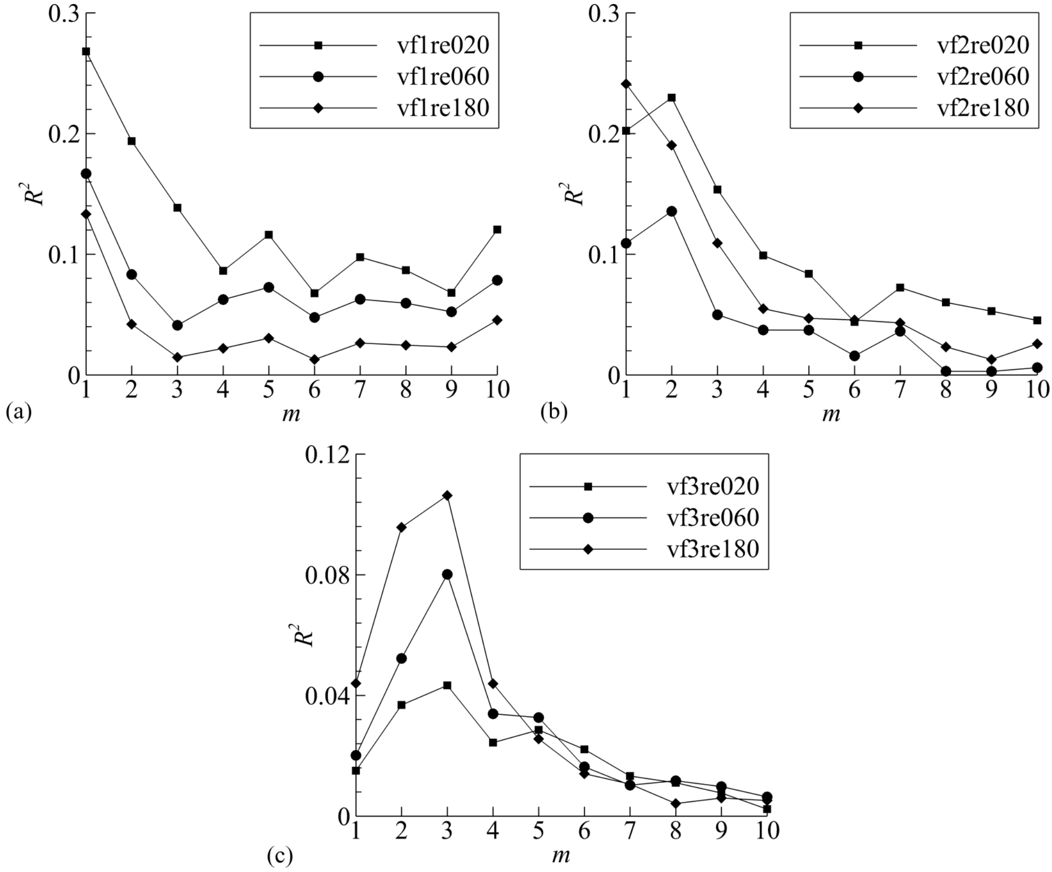

FIG. 17. Maximum coefficient of determination of the lift scatter data as a function of surrounding particles included for (a) $\phi = 0.11$, (b) $\phi = 0.21$, and (c) $\phi = 0.44$.

in Eqs. (6.9) and (6.10), where only the magnitude of lateral separation is taken into account. This is due to the fact that as far as drag is concerned only the lateral separation of the neighbor away from the streamwise axis of the reference particle is of interest. Different upstream neighbors with the same $\zeta_{L,u}$ but oriented differently on the y-z plane will affect the drag on the reference particle in an identical way, whereas such relative positions of the neighbor on the y-z plane will influence the

TABLE VIII. Number of spheres and the weights of the spatial parameters that result in the highest correlation with the lift scatter data.

Case	m	R^2	a	b	c	d
vf1re20	1	0.27	0	−0.75	0	0.25
vf1re60	1	0.17	0	−0.8	0.2	0
vf1re180	1	0.13	0.14	−0.57	−0.14	0.14
vf2re20	2	0.23	0.13	−0.63	−0.13	0.13
vf2re60	2	0.14	0.2	−0.8	0	0
vf2re180	1	0.19	−0.1	−0.5	0.3	−0.1
vf3re20	3	0.04	0.25	−0.5	−0.25	0
vf3re60	3	0.08	0.1	−0.5	0.3	0.1
vf3re180	3	0.11	0	−0.625	0.25	0.125

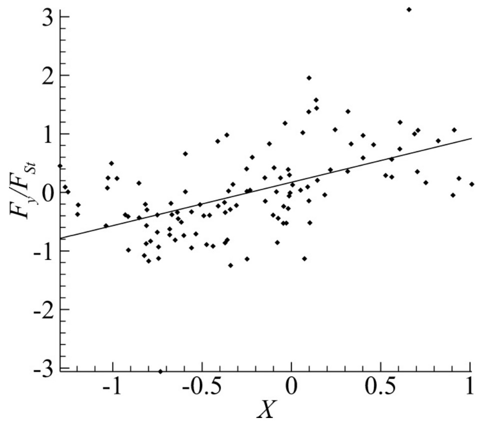

FIG. 18. Scatter plot of the actual lift in the spanwise direction vs X using the parameters listed in Table VIII for vf1re20 alongside the linear fit of the data. Here $R^2 = 0.27$.

direction of the transverse force. For example, two upstream neighbors with the same streamwise and transverse separation magnitudes, but one displaced along the positive y axis and the other displaced along the negative y axis, could additively contribute to the drag force variation from the mean, but their influence on the transverse force should cancel by symmetry. The simple definitions (6.16) and (6.17) are to preserve such symmetry.

Similar to the analysis performed in Sec. VI C 2 a, a scatter plot of X vs F_y is obtained, where X is the effective neighborhood parameter calculated from Eq. (6.15), using the parameters from Eqs. (6.18), (6.19), (6.11), and (6.12). The lateral force F_y is obtained from the DNSs as $F_y = \boldsymbol{F}_n \cdot \boldsymbol{e}_y$. Figure 17 shows the maximum R^2 obtained for each m and the optimum values of the weights a, b, c, and d. The results show that for increasing volume fractions, more spheres need to be included to reach the highest correlation. Table VIII includes the optimal weights that result in the highest R^2 value for each case. Their relative magnitudes and sign provide information on the relative importance of these parameters and the manner in which they influence the variation of the hydrodynamic lift force. Figure 18 shows the scatter plot of case vf1re20, which provides a good qualitative representation for all the cases considered. The following interpretations can be deduced:

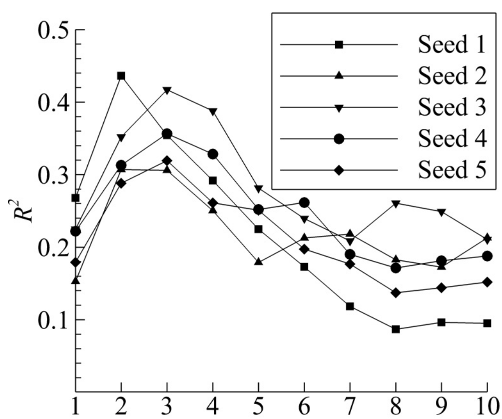

FIG. 19. Maximum coefficient of determination of the drag scatter data as a function of surrounding particles included for different distributions of case vf2re20.

TABLE IX. Number of spheres and the weights of the spatial parameters that result in the highest correlation with the drag scatter data for different distributions of spheres for case vf2re20.

vf2re20	m	a	b	c	d
seed 1	2	0.42	−0.08	0.17	−0.33
seed 2	2	0.50	0.30	0	−0.20
seed 3	3	0.46	0.27	0.09	−0.18
seed 4	3	0.36	0.09	0.18	−0.36
seed 5	3	0.67	0.167	0	−0.17

(i) The most dominant parameter in all cases shown is the effective lateral gap between the reference sphere and the neighboring particles located upstream $\zeta_{L,u}$. The negative value of the weight b indicates that if the neighbors are located with an effective lateral position with respect to the reference sphere, they would induce a lateral force in the direction opposite to the effective lateral position.

(ii) The other three spatial parameters $\zeta_{L,d}$, $\zeta_{S,u}$, and $\zeta_{S,d}$ have only an insignificant effect on the lift force.

(iii) The correlation of the nonisotropic spatial parameter X with the lift force decreases for higher volume fraction. For the highest volume fraction tested, the correlation is almost nonexistent.

(iv) In some cases, only one particle upstream and one downstream are responsible for dictating the lift variation on a sphere.

The particles located upstream have the main role in channeling the flow toward the reference sphere and determining its angle of impact. Referring to Fig. 15(a), it can be seen that for each particle, the presence of the other particle creates an asymmetry in the pressure field in the lateral direction, which creates lift. The vortical structures generated by each particle [refer to Figs. 12(b) and 16] also play a major role in inducing a lift force. The importance of ambient vorticity in generating lift force on spheres at finite Re is well established [43–45].

The results presented in Sec. VI C are for one particular simulation for each case. The case of vf2re20 is repeated for five different distributions of spheres. Figure 19 shows the variation of the R^2 value with increasing m for the five different distributions of spheres tested. All cases exhibit the same general behavior, but the maximum correlation varies slightly in magnitude. Two of the cases considered show the maximum at $m = 2$ and the other three reach their maximum at $m = 3$. Table IX shows the optimal weights that result in the maximum correlation for the different distributions. The same general trend is observed in all the realizations where the dominant parameters are $\zeta_{L,d}$ and $\zeta_{S,u}$. This shows that the qualitative dependences described earlier are independent of the specific distribution of the array. Nonetheless, the optimal weights vary significantly in magnitude from one realization to another.

VII. CONCLUSION

In this study we identified the distribution of the drag and lift forces within an array of random monodisperse spherical particles. For the drag, the distribution is nearly Gaussian with a standard deviation that ranges between 17% and 26% of the mean drag. The ratio of the standard deviation with respect to the mean drag decreases when the volume fraction increases. The lateral force distribution showed a slightly higher kurtosis than a normal distribution, but not enough to suggest a strong deviation from the Gaussian distribution. For the lateral forces, the standard deviation ratio with respect to the mean drag showed a relatively stable value at around 14.5% for all volume fractions and Reynolds numbers. A simple point-particle model for quasisteady drag was presented that includes the identified force variation within the array.

An analysis of the parameters that governs the variation of the forces from one sphere to another has been conducted. Classic parameters such as the local volume fraction and the nth-nearest-neighbor showed little to no correlation with the variation of the drag and lift forces. It was also shown that an anisotropic measure of the neighborhood would correlate better with the hydrodynamic forces since the flow is nonisotropic in nature.

A neighborhood measure that assigns different weights to different spatial directions was introduced. The results showed that the variation of the drag is mostly influenced by the closest three to eight particles. The streamwise gap between a sphere and its upstream neighbors plays a major role in determining the drag variation. It was also shown that for small volume fractions and Reynolds number, the influence of the lateral gap between a particle and its downstream neighbors on the drag variation is significant. The lift variation has been shown to be dictated by the lateral location of the closest one to two neighboring spheres located upstream of each reference particle. The significance and influence of the spatial measures in different directions were shown to be related to the pressure and vorticity fields surrounding a single sphere in an ambient flow. The results also show that for a densely packed array, the correlation of the drag and lateral force variation with any linear spatial measure decreases tremendously.

The statistics presented in Sec. VI A and the qualitative analysis presented in Sec. VI C 2 are independent of the specific distribution used in the analysis and are a characteristic of any particle distribution with the same volume fraction and Reynolds number. The point-particle model given by Eq. (6.5) reflects the actual statistical scatter within the array. The correlation with the nonisotropic measure shown in Sec. VI C is meant be a qualitative description to demonstrate the possibility of developing improved point-particle models based on spatial measures that correlate better with the real drag and lift forces. More work is still needed before achieving a working robust model that can quantitatively predict the actual drag and lift on each particle based on the sole knowledge of the location of the particles and the macroscale flow. Such a model would be able to reflect the actual drag and lift variation without the need to include stochastic forcing.

ACKNOWLEDGMENTS

This work was supported by the US Department of Energy, National Nuclear Security Administration, Advanced Simulation and Computing Program, as a Cooperative Agreement to the University of Florida under the Predictive Science Academic Alliance Program, under Contract No. DE-NA0002378. Additionally, this work benefited from the National Science Foundation (NSF OISE-0968313) under Partnership for International Research and Education (PIRE) in Multiphase Flows at the University of Florida. TLJ was also supported in part by the Defense Threat Reduction Agency, Basic Research Award No. HDTRA1-14-1-0031 to University of Florida; SB was also supported in part by the Defense Threat Reduction Agency, Basic Research Award No. HDTRA1-14-1-0028 to University of Florida; Dr. Allen Dalton, program manager.

APPENDIX

Beetstra *et al.* [11], Tenneti *et al.* [13], Zaidi *et al.* [14], Bogner *et al.* [12], and Tang *et al.* [15] presented correlations of the mean drag with the volume fraction and particle Reynolds number for a random cluster of spherical particles. These correlations are listed here for convenience:

$$F_{BE}(\phi,\mathrm{Re}_p) = \frac{10\phi}{(1-\phi)^3} + (1-\phi)(1+1.5\sqrt{\phi}) + \frac{0.413\mathrm{Re}_p}{24(1-\phi)^3}\left[\frac{(1-\phi)^{-1}+3\phi(1-\phi)+8.4\mathrm{Re}_p^{-0.343}}{1+10^{3\phi}\mathrm{Re}_p^{-(1+4\phi)/2}}\right], \tag{A1}$$

$$F_{TE}(\phi,\mathrm{Re}_p) = \frac{1+0.15\,\mathrm{Re}_p^{0.687}}{(1-\phi)^3} + \frac{5.81\phi}{(1-\phi)^3} + 0.48\frac{\phi^{1/3}}{(1-\phi)^4} + \phi^3\mathrm{Re}_p\left(0.95+\frac{0.61\phi^3}{(1-\phi)^2}\right), \tag{A2}$$

$$F_{ZA}(\phi,\mathrm{Re}_p) = \begin{cases} \frac{10\phi}{(1-\phi)^3} + (1-\phi)(1+1.5\sqrt{\phi}) + \frac{0.034}{(1-\phi)^{3.7}}\mathrm{Re}_p, & \mathrm{Re}_p \leqslant 200 \\ \frac{10.9\phi^{0.4}}{(1-\phi)^{2.7}} + \frac{0.024}{(1-\phi)^{3.86}}\mathrm{Re}_p, & \mathrm{Re}_p > 200, \end{cases} \tag{A3}$$

$$F_{BO}(\phi,\mathrm{Re}_p) = (1-\phi)^{-5.726}[1.751 + 0.151\,\mathrm{Re}_p^{0.684} - 0.445(1+\mathrm{Re}_p)^{1.04\phi} - 0.16(1+\mathrm{Re}_p)^{0.0003\phi}], \tag{A4}$$

$$F_{TA}(\phi,\mathrm{Re}_p) = \frac{10\phi}{(1-\phi)^3} + (1-\phi)(1+1.5\sqrt{\phi}) + \left[0.11\phi(1+\phi) - \frac{0.00456}{(1-\phi)^4} + \left(0.169(1-\phi) + \frac{0.0644}{(1-\phi)^4}\right)\mathrm{Re}_p{}^{-0.343}\right]\frac{\mathrm{Re}_p}{1-\phi}. \tag{A5}$$

---

[1] J. H. Prévost, Mechanics of continuous porous media, Int. J. Eng. Sci. **18**, 787 (1980).
[2] S. Balachandar and J. K. Eaton, Turbulent dispersed multiphase flow, Annu. Rev. Fluid Mech. **42**, 111 (2010).
[3] S. Balachandar, A scaling analysis for point-particle approaches to turbulent multiphase flows, Int. J. Multiphase Flow **35**, 801 (2009).
[4] Y. Ling, M. Parmar, and S. Balachandar, A scaling analysis of added-mass and history forces and their coupling in dispersed multiphase flows, Int. J. Multiphase Flow **57**, 102 (2013).
[5] M. R. Maxey and J. J. Riley, Equation of motion for a small rigid sphere in a nonuniform flow, Phys. Fluids **26**, 883 (1983).
[6] R. J. Hill, D. L. Koch, and A. J. C. Ladd, The first effects of fluid inertia on flows in ordered and random arrays of spheres, J. Fluid Mech. **448**, 213 (2001).
[7] J. Magnaudet and I. Eames, The motion of high-Reynolds-number bubbles in inhomogeneous flows, Annu. Rev. Fluid Mech. **32**, 659 (2000).
[8] H. P. G. Darcy, *Les Fontaines Publiques de la Ville de Dijon* (Dalmont, Paris, 1856), Appendix, Note D.
[9] P. Forchheimer, Wasserbewegung durch boden, Z. Ver. Deutsch. Ing. **45**, 1782 (1901).
[10] J. F. Richardson and W. N. Zaki, The sedimentation of a suspension of uniform spheres under conditions of viscous flow, Chem. Eng. Sci. **3**, 65 (1954).
[11] R. Beetstra, M. A. Van der Hoef, and J. A. M. Kuipers, Drag force of intermediate Reynolds number flow past mono- and bidisperse arrays of spheres, AIChE J. **53**, 489 (2007).
[12] S. Bogner, S. Mohanty, and U. Rüde, Drag correlation for dilute and moderately dense fluid-particle systems using the lattice Boltzmann method, Int. J. Multiphase Flow **68**, 71 (2015).
[13] S. Tenneti, R. Garg, and S. Subramaniam, Drag law for monodisperse gas-solid systems using particle-resolved direct numerical simulation of flow past fixed assemblies of spheres, Int. J. Multiphase Flow **37**, 1072 (2011).
[14] A. A. Zaidi, T. Tsuji, and T. Tanaka, A new relation of drag force for high Stokes number monodisperse spheres by direct numerical simulation, Adv. Powder Technol. **25**, 1860 (2014).
[15] Y. Tang *et al.*, A new drag correlation from fully resolved simulations of flow past monodisperse static arrays of spheres, AIChE J. **61**, 688 (2015).
[16] G. K. Batchelor, Sedimentation in a dilute dispersion of spheres, J. Fluid Mech. **52**, 245 (1972).
[17] R. J. Hill, D. L. Koch, and A. J. C. Ladd, Moderate-Reynolds-number flows in ordered and random arrays of spheres, J. Fluid Mech. **448**, 243 (2001).
[18] D. Z. Zhang and A. Prosperetti, Averaged equations for inviscid disperse two-phase flow, J. Fluid Mech. **267**, 185 (1994).
[19] R. Jackson, Locally averaged equations of motion for a mixture of identical spherical particles and a Newtonian fluid, Chem. Eng. Sci. **52**, 2457 (1997).

[20] S. Whitaker, The Forchheimer equation: A theoretical development, Transp. Porous Media **25**, 27 (1996).
[21] T. B. Anderson and R. Jackson, Fluid mechanical description of fluidized beds. Equations of motion, Ind. Eng. Chem. Fund. **6**, 527 (1967).
[22] C. T. Crowe, J. D. Schwarzkopf, M. Sommerfeld, and Y. Tsuji, *Multiphase Flows with Droplets and Particles* (CRC, Boca Raton, 2011).
[23] S. Subramaniam, Lagrangian-Eulerian methods for multiphase flows, Prog. Energy Combust. Sci. **39**, 215 (2013).
[24] A. S. Berrouk *et al.*, Stochastic modelling of inertial particle dispersion by subgrid motion for LES of high Reynolds number pipe flow, J. Turbul. **8**, N50 (2007).
[25] J. Pozorski and S.V. Apte, Filtered particle tracking in isotropic turbulence and stochastic modeling of subgrid-scale dispersion, Int. J. Multiphase Flow **35**, 118 (2009).
[26] M. Uhlmann, An immersed boundary method with direct forcing for the simulation of particulate flows, J. Comput. Phys. **209**, 448 (2005).
[27] W. Anthony, A DEM-DLM/FD method for direct numerical simulation of particulate flows: Sedimentation of polygonal isometric particles in a Newtonian fluid with collisions, Comput. Fluids **38**, 1608 (2009).
[28] V. Topin *et al.*, Micro-rheology of dense particulate flows: Application to immersed avalanches. J. Non-Newtonian Fluid Mech. **166**, 63 (2011).
[29] A. G. Kidanemariam and M. Uhlmann, Interface-resolved direct numerical simulation of the erosion of a sediment bed sheared by laminar channel flow, Int. J. Multiphase Flow **67**, 174 (2014).
[30] Y. Matsumura and T. L. Jackson, Numerical simulation of fluid flow through random packs of cylinders using immersed boundary method, Phys. Fluids **26**, 043602 (2014).
[31] C. Canuto, M. Y. Hussaini, A. Quarteroni, and T. A. Zang, *Spectral Methods in Fluid Dynamics*, Springer Series in Computational Physics (Springer, Berlin, 1988).
[32] T. A. Cortese and S. Balachandar, High performance spectral simulation of turbulent flows in massively parallel machines with distributed memory, Int. J. High Perform. Comput. Appl. **9**, 187 (1995).
[33] A. M. Roma, C. S. Peskin, and M. J. Berger, An adaptive version of the immersed boundary method, J. Comput. Phys. **153**, 509 (1999).
[34] G. Akiki and S. Balachandar, Immersed boundary method with non-uniform distribution of Lagrangian markers for a non-uniform Eulerian mesh, J. Comput. Phys. **307**, 34 (2016).
[35] A. Pinelli, I. Z. Naqavi, U. Piomelli, and J. Favier, Immersed-boundary methods for general finite-difference and finite-volume Navier-Stokes solvers, J. Comput. Phys. **229**, 9073 (2010).
[36] E. J. Hinch, An averaged-equation approach to particle interactions in a fluid suspension, J. Fluid Mech. **83**, 695 (1977).
[37] Y. Tang *et al.*, A methodology for highly accurate results of direct numerical simulations: Drag force in dense gas-solid flows at intermediate Reynolds number, Int. J. Multiphase Flow **62**, 73 (2014).
[38] J. Quintanilla and S. Torquato, Local volume fraction fluctuations in random media, J. Chem. Phys. **106**, 2741 (1997).
[39] K. Yazdchi, S. Srivastava, and S. Luding, Micro-macro relations for flow through random arrays of cylinders, Compos. Part A: Appl. Sci. **43**, 2007 (2012).
[40] A. C. Thompson, *Minkowski Geometry, Volume 63 of Encyclopedia of Mathematics and its Applications* (Cambridge University Press, Cambridge, 1996).
[41] M. Stimson and G. B. Jeffery, The motion of two spheres in a viscous fluid, Proc. R. Soc. London Ser. A **111**, 110 (1926).
[42] G. K. Batchelor and J.-T. Green, The hydrodynamic interaction of two small freely-moving spheres in a linear flow field, J. Fluid Mech. **56**, 375 (1972).
[43] P. G. T. Saffman, The lift on a small sphere in a slow shear flow, J Fluid Mech. **22**, 385 (1965).
[44] R. Kurose and S. Komori, Drag and lift forces on a rotating sphere in a linear shear flow, J. Fluid Mech. **384**, 183 (1999).
[45] P. Bagchi and S. Balachandar, Shear versus vortex-induced lift force on a rigid sphere at moderate *Re*, J. Fluid Mech. **473**, 379 (2002).